JGR Space Physics

METHOD
10.1029/2022JA030369

Quantifying the Sheath Impedance of the Electric Double Probe Instrument on the Van Allen Probes

D. P. Hartley[1], I. W. Christopher[1], C. A. Kletzing[1], W. S. Kurth[1], O. Santolik[2,3], I. Kolmasova[2,3], J. R. Wygant[4], and J. W. Bonnell[5]

[1]Department of Physics and Astronomy, University of Iowa, Iowa City, IA, USA, [2]Department of Space Physics, Institute of Atmospheric Physics, Prague, Czech Republic, [3]Faculty of Mathematics and Physics, Charles University, Prague, Czech Republic, [4]School of Physics and Astronomy, University of Minnesota, Minneapolis, MN, USA, [5]Space Sciences Laboratory, University of California, Berkeley, CA, USA

Key Points:

- Variable coupling impedance between the instrument and plasma has been quantified for the electric field measurements on Van Allen Probes
- Sheath correction is demonstrated to substantially improve agreement between data and theoretical predictions from Faraday's Law
- Sheath-corrected EMFISIS L4 data set produced for archive. Full details are also provided to facilitate manual data corrections

Supporting Information:

Supporting Information may be found in the online version of this article.

Correspondence to:

D. P. Hartley,
david-hartley@uiowa.edu

Citation:

Hartley, D. P., Christopher, I. W., Kletzing, C. A., Kurth, W. S., Santolik, O., Kolmasova, I., et al. (2022). Quantifying the sheath impedance of the electric double probe instrument on the Van Allen Probes. *Journal of Geophysical Research: Space Physics*, *127*, e2022JA030369. https://doi.org/10.1029/2022JA030369

Received 8 FEB 2022
Accepted 21 APR 2022

Abstract Spherical double probe electric field sensors become electrically coupled to magnetospheric plasma during operation, leading to an instrument response that varies with the local plasma environment. Here, a method is developed for determining this variable coupling impedance for each measurement direction by using periods of favorable boom, wave, and magnetic field geometry. Comparing electric field complex amplitudes between 30 Hz and 10 kHz observed along each boom direction to those predicted from simultaneous magnetic field measurements and cold plasma theory allows for the amplitude and phase response of the instrument to be quantified over the full range of plasma densities encountered on-orbit. A sheath model is developed to describe how the sheath resistance, sheath capacitance, and relative effective length vary as a function of plasma density. An additional empirical correction is also included to describe the phase response along the spin-axis. The modeled sheath correction is subsequently tested for case studies of burst-mode data and statistical analyses of survey-mode data. It is demonstrated that the levels of agreement between observations and theoretical predictions based on Faraday's Law are substantially greater for the sheath corrected data than for uncorrected observations. Comparisons between observations with oppositely directed Poynting vector directions reveals that the sheath correction reconciles a bifurcated distribution in the uncorrected data to a single peak centered on agreement with Faraday's Law. A full sheath corrected EMFISIS L4 survey mode data set has been produced for final archive. Full details of the sheath correction are also provided for manual data correction.

1. Introduction

The wave electric field in the magnetosphere is typically measured by spherical double probe sensors mounted on long booms (e.g., S3-3 (Mozer et al., 1979), ISEE-1 (Mozer, 1973), CRRES (Wygant et al., 1992), Viking (Marklund, 1993), Freja (Marklund et al., 2004), FAST (Ergun et al., 2001), Polar (Harvey et al., 1995), Cluster (Gustafsson et al., 1997), and THEMIS (Bonnell et al., 2008)). The Electric Field and Waves (EFW) instrument (Wygant et al., 2013) on the twin NASA Van Allen Probes spacecraft (Mauk et al., 2012) is no different, with centrifugally deployed long wire booms deployed in the spin plane (U and V directions) and shorter rigid booms deployed along the axis of the spinning spacecraft (W direction). The measurements take place at the end of these booms, with fine wire and spherical sensors separated by 100 m taking observations along the U and V axes, and spherical sensors separated by 14 m taking observations along the W axis. In this paper we consider corrections to the amplitude and phase of electric field measurements made by the EMFISIS Waves instrument (Kletzing et al., 2013) with the EFW electric field double probe sensors using the Waves search coils and waveform receiver (WFR).

The electric field along each axis is measured by considering the difference in potential, ΔV, between two sensors. The electric field is $\Delta V/L_{eff}$, where L_{eff} is the effective length of the boom. For spherical double probes L_{eff} is typically the separation distance between the two sensors. This is true for the majority of the plasma environments encountered by the Van Allen Probes spacecraft, but may not be true in the low-density case. In plasma where the temperature may be high, and the plasma density low, the Debye length, λ_D, increases as $\lambda_D = \left(\epsilon_0 k_B T/ne^2\right)^{1/2}$. If λ_D is comparable to the electric field instrument length scale, the effective length reduces to some fraction of the physical separation between the sensors, yielding a shorter effective length. Under these circumstances, a shorting factor, s_f, may be introduced in order to counteract this effect (e.g., Califf & Cully, 2016; Cully et al., 2007;

Khotyaintsev et al., 2014; Lejosne & Mozer, 2019; Pedersen et al., 1998; Mozer et al., 1974). Bonnell et al. (2008) estimated a shorting factor in the magnetosheath for THEMIS EFI by comparing the measured electric field to that calculated from ion velocity and the magnetic field observations, yielding a value of 0.69 (indicating an under measurement of the real electric field), as well as observations of shorting factors between 0.63 and 0.77 during a calibration campaign on THEMIS-C. We do note however that the double probe separation distance on THEMIS was considerably smaller than it is on Van Allen Probes. With the instrumentation on board the Van Allen Probes, the W axis is more susceptible than the U and V axis to this shorting effect, given the significantly shorter tip-to-tip sensor separation.

The electric field sensors become electrically coupled to the plasma as they operate in the near-Earth environment, meaning that the electric field measurements are subject to fluctuations in the on-orbit plasma conditions (e.g., Fahleson, 1967; Koons et al., 1970; Storey, 1963). This instrument-plasma coupling can be simply represented by a voltage divider with complex impedance (e.g., Bale et al., 2008; Boehm et al., 1994; Gurnett, 1998), where the input voltage is EL_{eff}, the voltage divider attenuates the signal, and the output voltage measured by the instrument is reduced to some fraction of the input voltage. The attenuation factor may be determined by impedance division, $\Delta V_{out}/\Delta V_{in} = Z_L/(Z_S + Z_L)$, where Z_L is the known load impedance on the spacecraft side of the circuit and Z_S is the sheath impedance dictated by the plasma environment in which the spacecraft is operating. Note that here, impedance, Z, is the parallel combination of a resistor and a capacitor; $1/Z = 1/R + j\omega C$, where R is resistance, j is the imaginary unit, ω is the angular frequency ($2\pi f$), and C is capacitance.

The frequency of the incident waves also plays a role in the instrument response. The resistance dominates the impedance division for low frequency waves, meaning that the signal attenuation is approximately $\Delta V_{out}/\Delta V_{in} = R_L/(R_S + R_L)$. Since the load resistance of the spacecraft (~1 $T\Omega$ for Van Allen Probes) is typically much greater than the sheath resistance, $R_L \gg R_S$, the impedance division goes to unity, yielding no signal attenuation, $V_{out} = EL_{eff}$. For high frequency waves the impedance division may be simplified to capacitive coupling, giving a signal attenuation of $\Delta V_{out}/\Delta V_{in} = C_S/(C_S + C_L)$. In the ideal case that $C_S \gg C_L$, there is no signal attenuation. However, in practice, this capacitive division typically yields values on the order of 0.6. For intermediate wave frequencies a transition region between resistive and capacitive coupling occurs, known as the R-C transition region, where the response of the instrument varies with frequency. This yields a frequency dependent response function that impacts both amplitude and phase of the electric field observations. Accounting for both the sheath impedance, and the shorting factor, yields a response function that may be described as $s_f Z_L/(Z_S + Z_L)$.

In previous studies, a technique was developed for using magnetic field observations of whistler-mode waves and the cold plasma dispersion relation to predict the electric field (Hartley et al., 2015, 2016, 2017). This predicted electric field was subsequently compared to the observed electric field in order to determine the on-orbit response function of Van Allen Probes electric field observations. However, in these studies the correction factor was only applicable to the total observed electric field amplitude summed over all measurement directions, whereas practically speaking the response of each boom/sensor type (U/V or W) is different. Additionally, no phase corrections were made. While this is preliminary work was useful for correcting the total electric field wave amplitude, it is not useful for correcting the direction of the electric field vector, or for correcting derivative electric field properties such as the Poynting vector. Here, we develop a technique of using periods of favorable boom, wave, and magnetic field geometry to quantify the sheath impedance for each boom/sensor measurement direction separately.

2. Method

First, whistler-mode waves are isolated by imposing threshold values such that the ellipticity (Santolík et al., 2002) and the 2D degree of coherence in the polarization plane (Santolík & Gurnett, 2002) of the waves must both exceed 0.5, meaning right-hand polarized waves. The planarity (Santolík et al., 2003) of the waves must also exceed 0.6. This planarity threshold, coupled with the ellipticity threshold, ensures no more than 10% of the total power is outside of the plane of polarization (Hartley et al., 2018) and the wave normal direction determined using Singular Value Decomposition (Santolík et al., 2003) is well-defined. Note that ellipticity, 2D degree of coherence, and planarity are all determined using magnetic field observations from the search coil magnetometers. Additionally, the wave power must exceed a multiple of five times the instrument background levels as listed at https://emfisis.physics.uiowa.edu/Events/rbsp-a/backgrounds/ and emfisis.physics.uiowa.edu/Events/

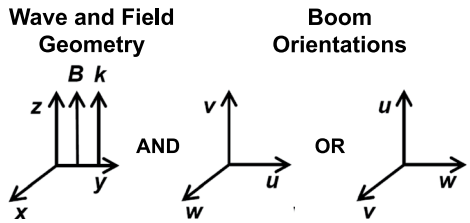

Figure 1. Schematic showing the time periods of favorable geometry that are used for this analysis.

rbsp–b/backgrounds/. This selection criteria is deemed to provide a satisfactory balance between ensuring the validity of the techniques used (e.g., SVD requires the plane wave approximation) and ensuring sufficient data over a broad range of plasma density values to accurately quantify the sheath impedance effects.

The methodology used here utilizes time periods of favorable geometry between the wave vector, k, the background magnetic field, B_0, and the electric field boom directions. First, the angle between k and B_0, defined as θ_k, must be less than 15°. For these time periods, the assumption of parallel propagation is valid and therefore Faraday's Law yields; $B_x = -kE_y/\omega$, $B_y = kE_x/\omega$, and $B_z = 0$ where B_x, B_y and B_z are complex Fourier coefficients at angular frequency, ω, of the wave magnetic field, and the z-direction is aligned with B_0. With the assumption that $f_{ci} \ll f$ and the cold plasma approximation are valid for the wave frequencies and plasma conditions where whistler-mode waves occur, the components of the whistler-mode wave electric field may be calculated from magnetic field observations using Equations 1 and 2.

$$E_x = \frac{\omega}{k} B_y = \frac{c}{\sqrt{1 - \frac{f_{pe}^2}{f(f - f_{ce})}}} B_y \tag{1}$$

$$E_y = -\frac{\omega}{k} B_x = -\frac{c}{\sqrt{1 - \frac{f_{pe}^2}{f(f - f_{ce})}}} B_x \tag{2}$$

where f_{ce} is the electron cyclotron frequency and f_{pe} is the electron plasma frequency.

Second, we further filter for time periods where the background magnetic field, B_0, is within 15° of either the U or V electric field measurement directions. Due to the orientation of the Van Allen Probes spacecraft, there are very few time periods where the W boom direction is aligned with the background magnetic field and as such, these time periods are not investigated in this study.

For the selected time periods of favorable geometry, note that the x and y directions used in expressing Faraday's Law are defined as lying parallel to the measurement directions of the electric field instrument as shown in Figure 1. That is, x and y are analogous to the W and U boom directions when the V boom is aligned with both B_0 and k. Conversely, the x and y directions are analogous to the V and W boom directions when the U boom is parallel with B_0 and k. As such, Equations 1 and 2 allow us to calculate the theoretically predicted whistler-mode wave electric field values along each of the boom directions, and directly compare these values to those measured by the EFW instrument.

To determine both the amplitude and phase response of the instrumentation, we can take Equations 1 and 2 and apply them to the complex amplitude of B to determine E. The complex amplitude of E_w and E_u are determined from B_u and B_w respectively when the V boom is aligned with both the background magnetic field and the k-vector, and E_w and E_v are determined from B_v and B_w respectively when the U boom is parallel or anti-parallel with the background magnetic field and the k-vector. These quantities are then compared to the complex amplitude of the electric field measured by the instrument. In EMFISIS survey mode the complex amplitudes from the Fourier transform of the waveform are not sent to the ground. However, the complex amplitudes may be determined from the spectral matrix, which is sent to the ground. Details on this calculation are provided in Appendix A. Applying Equations 1 and 2 to the complex amplitudes allows us to use observations of the magnetic field to explicitly determine the electric field instrument response in both amplitude and phase by calculating the complex ratio between the observed electric field and the calculated electric field.

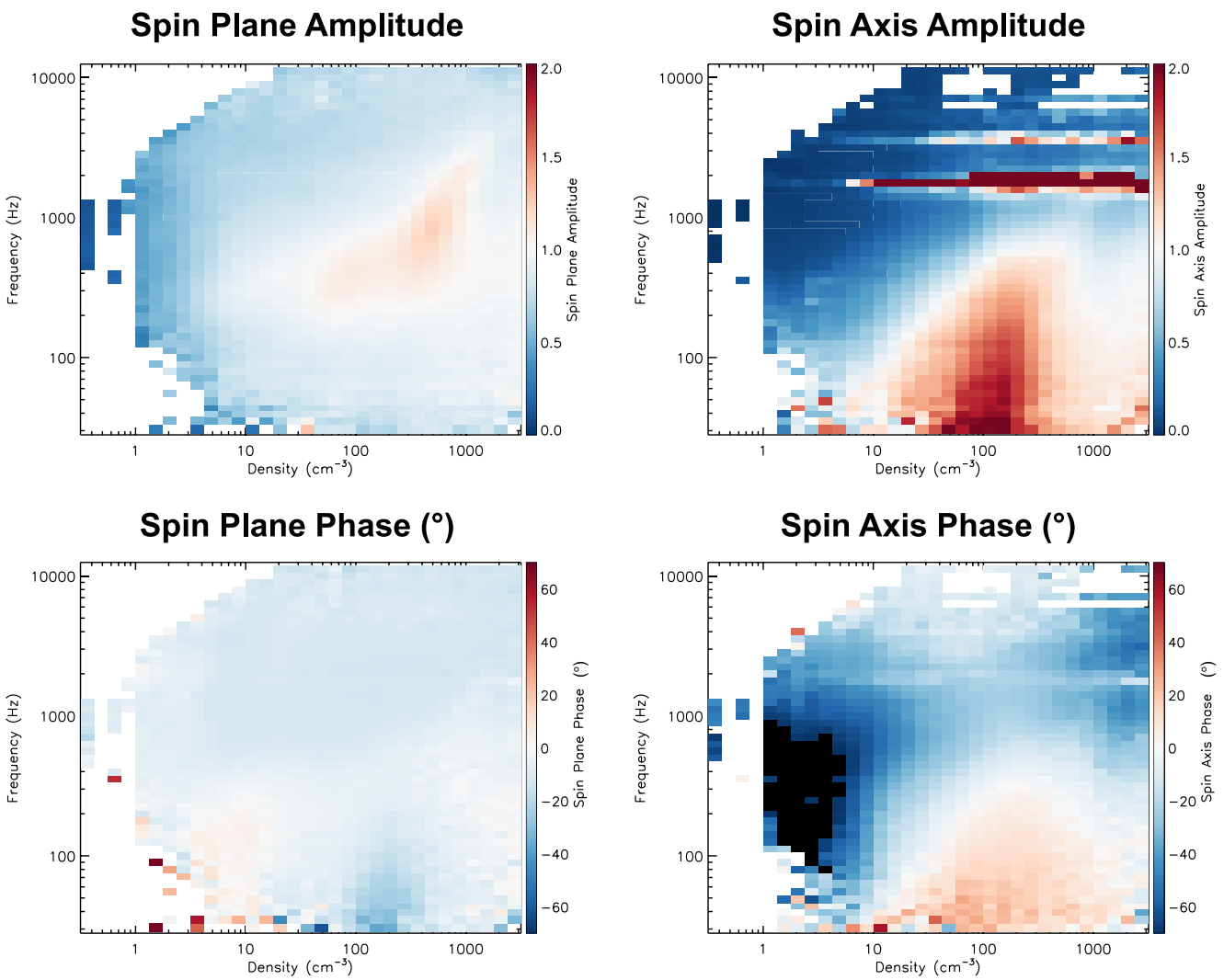

Figure 2. The median amplitude and phase of the complex amplitude ratio values as a function of wave frequency and plasma density.

3. Instrument Response and Determination of Correction Factors

To directly compare measurements to theory, the ratio of the observed whistler-mode wave electric field to the theoretically predicted electric field based on magnetic field observations is considered. The amplitude and phase of the complex amplitude ratio values are binned as a function of plasma density, for each of the logarithmically spaced frequency channels of the EMFISIS instrument. The plasma density is obtained from observations of the upper hybrid resonance line, as described in Kurth et al. (2015), for all of the analysis presented hereafter. Figure 2 shows the median amplitude of the ratio values as a function of frequency and plasma density for both the spin-plane U and V sensors (left), and the spin-axis W sensors (right). This format essentially shows the amplitude response function of each boom/sensor type, under the assumption that the theoretically predicted electric field is analogous to the real electric field, and by extension, the measured magnetic field is analogous to the real magnetic field. Any uncertainties in magnetic field observations would impact on the calculations presented here, however no such uncertainties have been identified, and any that do exist are likely to be of much lower order than those present in the electric field observations due to sheath impedance effects. Also shown in Figure 2 is the median phase of the ratio values, which is considered to be the phase response of each boom/sensor type.

For the spin-plane amplitude, the majority of density and frequency bins contain values less than unity as indicated by blue colors, meaning that the measured electric field is less than that predicted. These under-measure-

ments are largest in the low density case, with levels of agreement generally increasing with increasing density. Note that for frequencies between ~300 and 2,000 Hz at densities between ~50–1,000 cm^{-3} we see small gains in the measured electric field, where it is actually larger than that predicted, as indicated by red colors. We note that this behavior decreases substantially if the planarity threshold is increased, albeit at the expense of excluding significantly more data. For the spin-plane phase we generally observe only small deviations from what is expected (zero phase difference), with the majority of values being within about ±10°.

For the spin-axis amplitude, there are much greater deviations from a ratio of unity. At low density values the electric field measured by the instrument can be 10%, or less, of that predicted. As density increases, the magnitude of these underestimates generally decrease. Between density values of ~20 and 1,000 cm^{-3}, the amplitude of lower frequency waves (below ~1 kHz) is substantially over-measured when compared to theory, as indicated by red colors. In comparison to the spin-plane direction, this behavior cannot be decreased by increasing the planarity threshold. Note that the horizontal red features centered on 2 and 4 kHz are due to noise lines in the spin-axis spectra. For the spin-axis phase, in the same region where large over-measurements of the wave amplitude are observed, we see a positive phase difference. In the low-density regime, large negative phase differences are apparent, up to 70° or more. In general, outside the region where the wave amplitude is over-measured, it is apparent that the largest phase difference occurs roughly along a diagonal, increasing in frequency as density increases.

For both boom/sensor types, the structure is relatively consistent with that described by impedance division, as described in Section 1. For the amplitude response, lower frequencies typically have larger ratios that are closer to unity, where the resistance dominates the impedance division. By comparison, the electric field at higher frequencies is generally underestimated as would be expected in the capacitive coupling regime. For the phase response to be consistent with sheath impedance effects, we would expect the largest phase shifts to occur along the transition region between resistive and capacitive coupling, where the roll-off in the response is observed in the wave amplitude. This is particularly apparent in the spin-axis observations, along the diagonal, decreasing in density as frequency decreases.

To demonstrate that the relationship between the observed and predicted electric field as a function of frequency and density is consistent with impedance division, Figure 3 provides an example of this frequency-dependent amplitude (top) and phase (bottom) response for both the spin-plane (left) and spin-axis (right) measurement directions in the plasma density range between 56.2 cm^{-3} and 75.0 cm^{-3}. The circles show the median value, either amplitude or phase, with the error bars indicating the 25th and 75th percentiles. In small intervals of plasma density (logarithmically spaced density bins with a width of 0.125), fits of the form of impedance division with a shorting factor are performed using minimum chi-squared estimation. The free fitting parameters for the amplitude fits are the boom shorting factor, s_f, and the sheath impedance, Z_S, which includes both a capacitance, C_S, and a resistance, R_S. For the phase response we only use the free parameters of capacitance, C_S, and resistance, R_S. s_f does not affect the phase response so is not needed. The fits that minimize the chi-squared statistic are shown by solid black lines. We note that in the region where anomalous gains are observed in the measured electric field wave amplitude, the relative effective length, s_f, is allowed to be larger than unity, as is the case in the plasma density range shown in Figure 3.

For fitting to the spin axis phase, for certain plasma density values, it became apparent that the functional form of the phase was offset from the data. As such, in this region, we include an additional fitting parameter to the sheath impedance fits in order to improve agreement between the phase correction from the sheath impedance fits and the phase correction explicitly determined from the complex amplitude ratios. This additional empirical phase shift is included by adding a phase correction, λ_S, to the phase of the impedance division when performing the chi-squared fits. These additional phase shifts are only required in the same density region where anomalous gains are observed ($s_f > 1$), leading us to the conclusion that there is some yet-to-be-explained behavior in the spin-axis in this density regime that is beyond the capabilities of being modeled by the parallel combination of a resistor and a capacitor to obtain a sheath impedance function. These chi squared fits are shown by black lines in Figure 3. Without the inclusion of the additional phase shift, λ_S, only negative phase shifts are possible. In the plasma density range shown, it is apparent that including λ_S allows for the fit to more accurately represent the positive phase shifts observed at wave frequencies less than 200 Hz. For comparison, the amplitude and phase response for each measurement direction from the final sheath model, which is described below and has a smooth variation as a function of wave frequency and plasma density, are shown by red lines. For completeness, similar

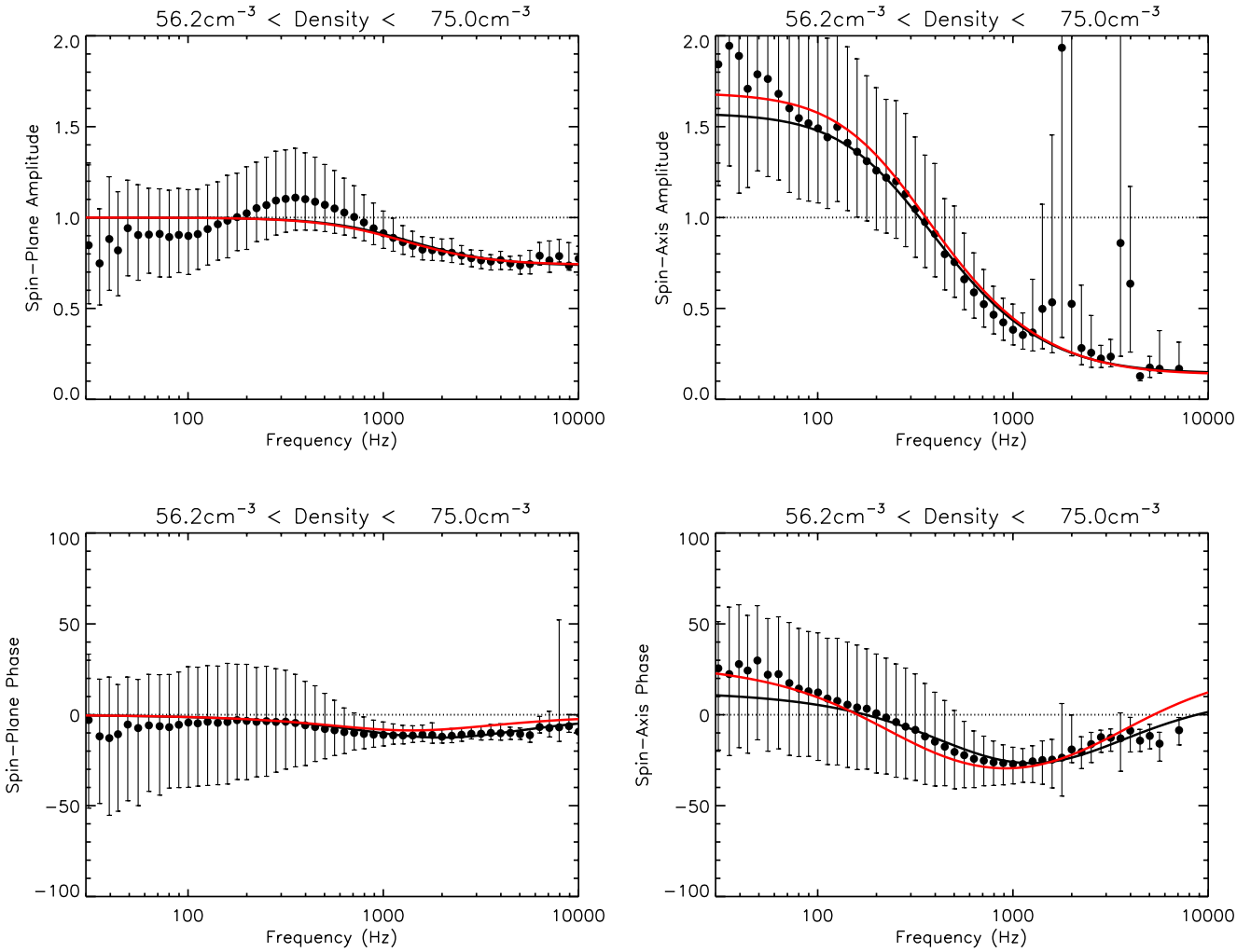

Figure 3. Examples of the minimized chi-squared fits (black lines) and the final sheath model fits (red lines) for both amplitude (top) and phase (bottom) for the spin-plane (left) and spin-axis (right) measurement directions.

plots showing the comparison between the final sheath impedance model and the amplitude and phase of the complex amplitude ratio values are provided for all density bins in supporting information.

The equations used for the chi-squared fits, and ultimately the final sheath impedance model, can be expressed with the following functional form;

$$\frac{E_{u,v,w}}{E^{cor}_{u,v,w}} = s_f \frac{Z_L}{(Z_S + Z_L)} \Lambda_S \tag{3}$$

where $E_{u,v,w}$ are the measured complex amplitudes and $E^{cor}_{u,v,w}$ are the sheath-corrected complex amplitudes (equivalent to the complex amplitudes calculated from Equations 1 and 2 when performing the chi-squared fits). It therefore follows that the sheath-corrected complex amplitudes, $E^{cor}_{u,v,w}$, may be obtained by dividing the measured complex amplitudes by $s_f \frac{Z_L}{(Z_S+Z_L)} \Lambda_S$.

The known load impedance on the spacecraft side of the circuit, Z_L, and the sheath impedance dictated by the plasma environment, Z_S, are determined through;

$$\frac{1}{Z_{L,S}} = \frac{1}{R_{L,S}} + j\omega C_{L,S} \tag{4}$$

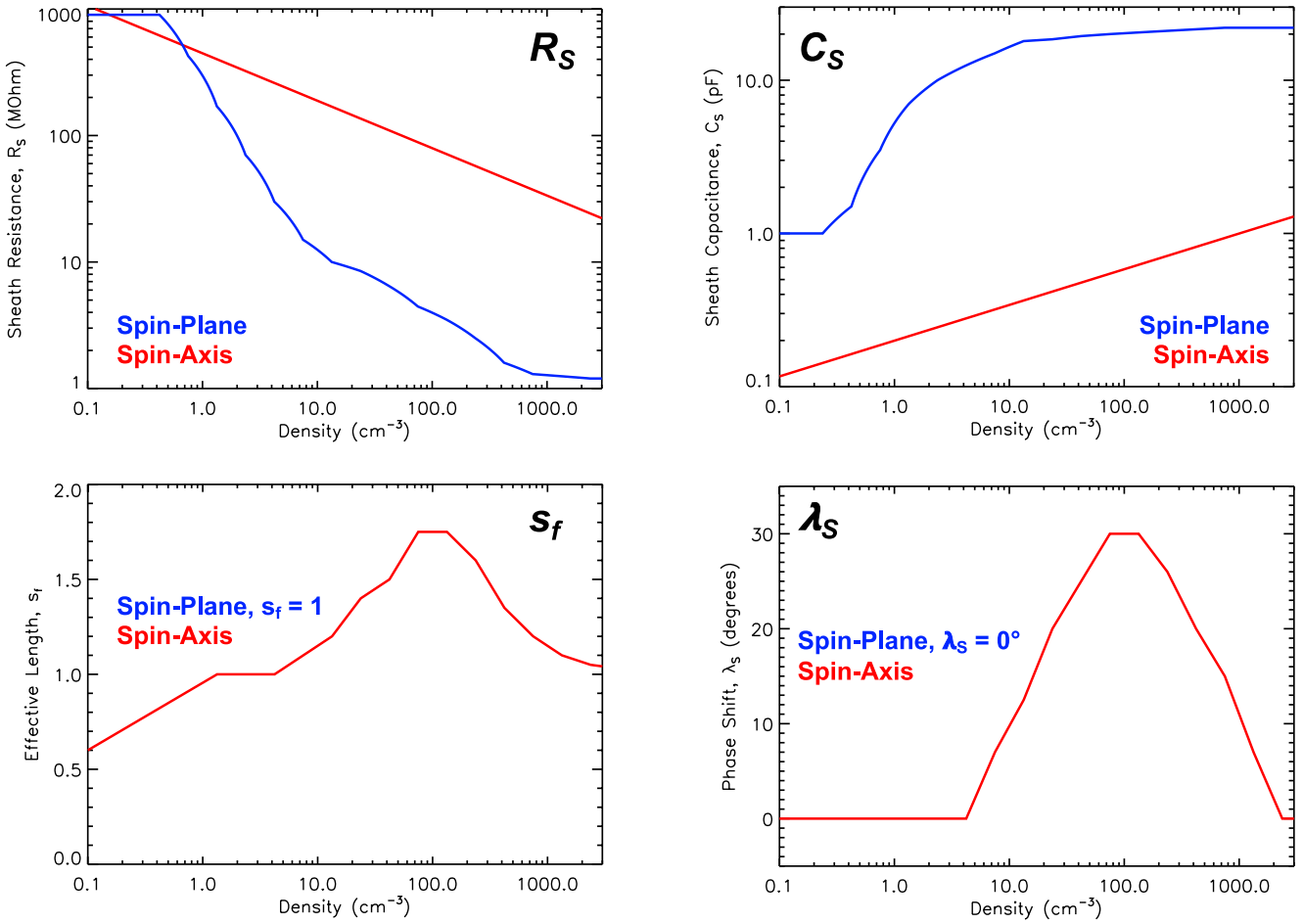

Figure 4. Sheath model coefficients; sheath resistance, R_S; sheath capacitance, C_S; effective length, s_f, and; phase shift, λ_S for the spin-plane (blue) and spin-axis (red).

Note that for the spin-plane direction $C_L = 7$ pF and $R_L = 1$ TΩ and for the spin-axis direction $C_L = 6$ pF and $R_L = 1$ TΩ. As discussed in Hartley et al. (2016), these values come from the pre-amplifier input stage and estimates from ground calibrations.

The additional phase shift is calculated by;

$$\Lambda_S = \cos\lambda_S + j\sin\lambda_S \tag{5}$$

where j is the imaginary unit. Note that for the spin-plane direction $\lambda_S = 0°$ for all plasma density values.

The fitting parameter values, s_f, R_S, C_S, and in the case of the phase response of the spin-axis, λ_S, that minimize chi-squared are subsequently considered as a function of plasma density. For each density bin, we obtain two values for each fitting parameter, one from the amplitude fit, and one from the phase fit. In general, these two values are in relatively close agreement. Manually, we consider the coefficients from both the amplitude and phase fits and produce a set of values that can be interpolated between, or, if appropriate, simple functional forms, to describe the variability in the fitting parameters as a function of plasma density. The result is that each of the fitting parameters are continuous variables as a function of plasma density for both boom/sensor types. Note that the shorting factor for the spin plane (U and V) is always approximated as unity. That is, this value does not vary as a function of plasma density. These smoothed values and/or functions are provided in Figure 4, allowing us to determine R_S, C_S, s_f, and λ_S, and therefore the instrument response, at all plasma density values encountered on orbit. A table of these values is provided as a function of plasma density in Appendix B.

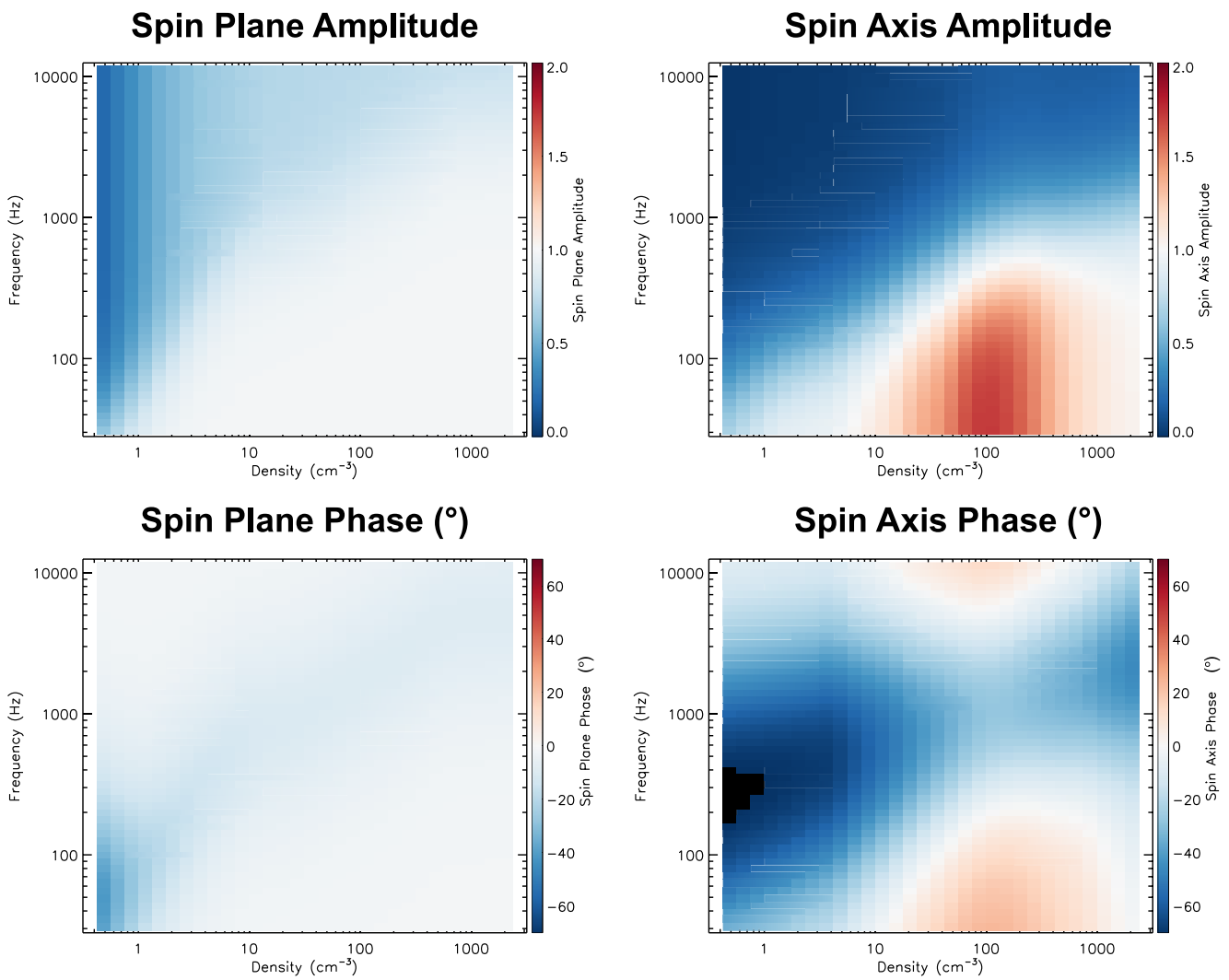

Figure 5. The final sheath impedance model describing the amplitude (top) and phase (bottom) corrections to be applied to the spin plane (left) and spin axis (right) measurements.

We note that the amplitude ratios greater than unity for the spin-axis between densities of ~60–1,000 cm^{-3} is not well understood, and is not predicted from the sheath model using the parallel combination of a resistor and a capacitor. Regardless, it is accounted for here by allowing s_f to be larger than unity. The additional phase shifts, λ_S, are only required in the density region where s_f is larger than unity. This potentially indicates some missing physics that cannot be accounted for with this impedance division setup.

Having obtained smoothly varying values as a function of plasma density, it is now possible to compute the variable coupling impedance between the instrument and the plasma at all plasma density values. Figure 5 shows the measurement response as a function of plasma density and wave frequency for the spin-plane (left) and spin-axis (right) for amplitude (top) and phase (bottom). Direct comparison to the raw ratio values provided in Figure 2 shows that these smoothly varying functions accurately describe the variability in the instrument response. An IDL routine to determine the correction factors given a set of plasma density and wave frequency values is provided in supporting information.

We note that in some instances the sheath model parameters determined here are far from what is expected from simple plasma sheath models. For example, R_S at low densities is somewhat larger than anticipated. With sensor bias current typically ~40 nA/sensor, and an assumed effective temperature of 1.5 eV for the emitted photoelectron distribution (although Pedersen (1995) described at least two characteristic photoelectron energies), the

sheath resistance should be approximately (1.5 eV)/(40 nA) ~38 MΩ, rather than the values as high as 900 MΩ obtained here. Additionally, the sheath capacitance values obtained at low densities are lower than expected. For a 4 cm radius spherical sensor, as used on Van Allen Probes, the vacuum capacitance is ~4 pF, whereas values less than this are obtained here. Finally, the relative effective length of the spin-plane booms is expected to drop below unity at low densities, whereas here, for simplicity, $s_f = 1$ is a constant for all density values. These deviations may be due to a number of reasons, including lower statistics and frequency coverage in the low density regime, equivalent fits possible for a range of different sheath coefficients, or missing physics in the implemented sheath model. These differences are the subject of ongoing investigations. The key result from this work is the transfer function itself, and the improved data quality that it can provide (as discussed in Section 4), rather than a full explanation of the sheath parameters and the physical processes driving uncertainties in electric field observations.

The complex sheath correction factors (correcting both wave amplitude and phase) are subsequently applied to all electric field observations that are above the noise floor. Appendix C details how the noise floor is determined for the specific purpose of applying the sheath corrections. To apply the correction, the measured complex amplitude of each electric field component is divided by the complex correction factor according to Equation 3. Conversely, the correction can be applied to the L2 spectral matrix values by following the steps described in Appendix D. The sheath-corrected electric field data are subsequently tested to determine the extent of the improvement (as described in Section 4).

4. Testing the Correction

Having obtained the sheath impedance corrections detailed above, a crucial step is to test the impact of these corrections against an expected outcome. Here, we consider a 1 second time period of continuous burst mode data from RBSP-A where EMFISIS Waves records waveforms of both E and B with a sampling rate of 35 kHz. Figure 6 shows this sample time period (2017-07-24 17:24:13.7 to 17:24:14.7), with a rising-tone chorus element clearly observable in both E and B spectrograms. The vertical pink line in Figure 6 highlights the time period of waveform data which will be used as a first test case to demonstrate the effects of the sheath correction.

A model electromagnetic whistler-mode wave is constructed using cold plasma theory, to compare with the observations. In the coordinate system where the z-axis is parallel to the background magnetic field, B_0, and the wave vector, k lies in the x-z plane with the angle between k and B_0 defined by θ_k, the x-component of the electric field is set by the time varying quantity $E_x = e^{i\omega t}$. The E_y and E_z components may then be determined by the cold plasma wave equation:

$$\begin{pmatrix} S - n^2\cos^2\theta_k & -iD & n^2\cos\theta_k\sin\theta_k \\ iD & S - n^2 & 0 \\ n^2\cos\theta_k\sin\theta_k & 0 & P - n^2\sin^2\theta_k \end{pmatrix} \begin{pmatrix} E_x \\ E_y \\ E_z \end{pmatrix} = 0 \quad (6)$$

The plasma parameters corresponding to the Van Allen Probes data observed during the test period ($f_{ce} = 4{,}250$ Hz and $f_{pe} = 22{,}200$ Hz in this case) are used when applying Equation 6. The wave frequency used for the model whistler-mode wave is determined from the peak in the magnetic field power spectrum observed during the test period, 1,207 Hz in this case. The magnetic field is then determined through Faraday's Law, yielding; $B_x = -\frac{k}{\omega}\cos\theta_k E_y$, $B_y = \frac{k}{\omega}(E_x\cos\theta_k - E_z\sin\theta_k)$, and $B_z = \frac{k}{\omega}\sin\theta_k E_y$, where θ_k is the wave normal angle determined from the data using SVD at the modeled wave frequency. This yields a set of E and B values in the x, y, z coordinate system, where the real part of these modeled quantities provides the model whistler-mode waveform. This model wave can then projected from the x, y, z coordinate system (where z is field-aligned and k is in the x-z plane) into the U, V, W boom/sensor coordinate system, to facilitate direct comparisons. Note that the data may also be projected onto the x, y, z coordinate system of the model.

The relative phase between all E and B components of the model are consistent with cold plasma theory, however there may be an absolute phase shift between the model and the data which needs to be accounted for. The phase difference between model and data is determined for all three components of B (which are not expected to require a phase correction due to sheath effects) by determining the phase of the complex amplitude ratio between data

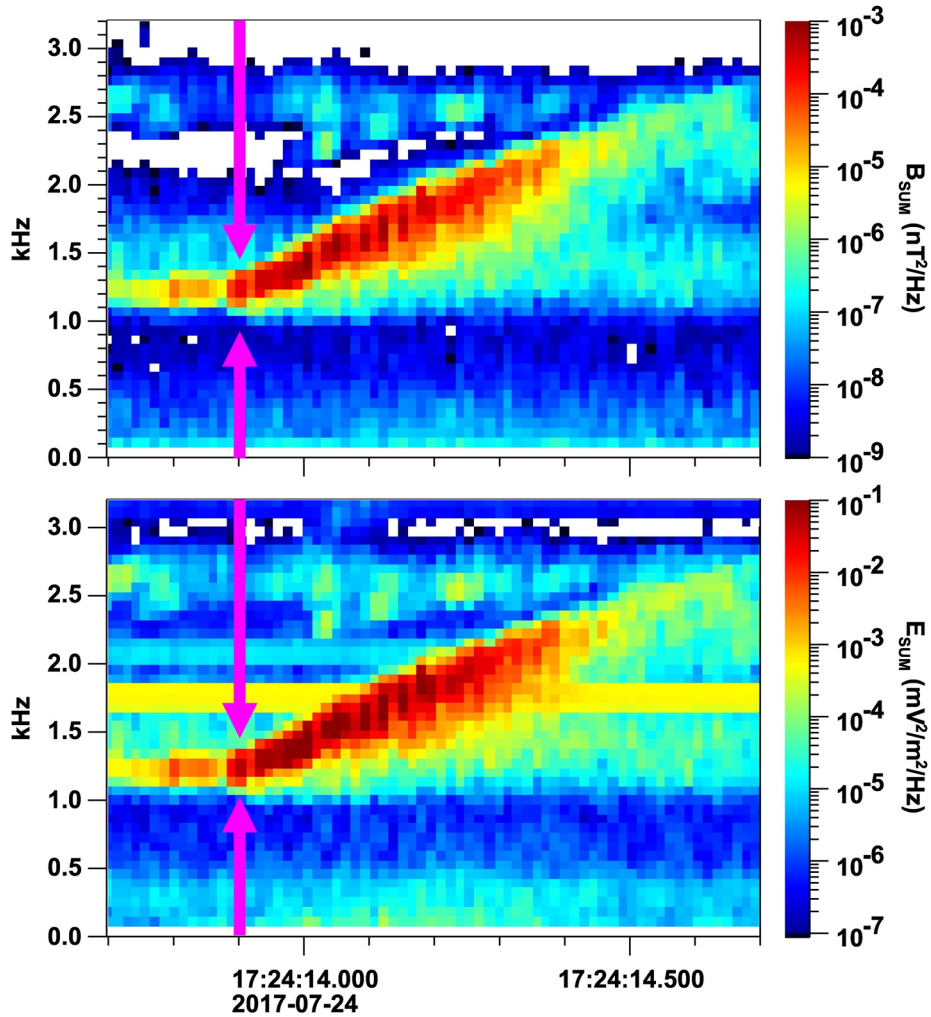

Figure 6. Spectrogram of the total magnetic (top) and electric (bottom) field wave power observed by RBSP-A on 2017-07-24 17:24:13.7 to 17:24:14.7.

and model. In this case, a phase difference between model and data of 169° is seen in B_u, 168° is seen in B_v, and 169° is seen in B_w. The average phase shift of 169° is then applied to all components of the modeled E and B to align the absolute phase of the model to the data, essentially setting the model to the same $t = t_0$ as the observations. The modeled magnetic field waveforms are multiplied by the total observed magnetic field wave amplitude at each time instance, $\sqrt{B_u(t)^2 + B_v(t)^2 + B_w(t)^2}$, such that the observed total magnetic field wave amplitude is equal to the modeled total magnetic field wave amplitude. For the electric field the multiplicative factor is given by the total electric field wave amplitude calculated from the total magnetic field wave amplitude, following Equation 2 of Hartley et al. (2016). This calculated quantity is used, as opposed to the measured total electric field wave amplitude, because the measured quantity is subject to the same sheath impedance effects that are being corrected. Both the observed and modeled wave are then normalized by the maximum wave amplitude observed during the interval.

The measured quantities are treated with an ideal bandpass filter (unity in the pass band, zero above and below the pass band) to isolate the desired signal, as well as to limit noise at other frequencies where significant power may exist. The boundaries of this bandpass filter are at 0.8 f and 1.2 f, where f is the wave frequency where the peak in the total magnetic field power spectrum is observed during the test period, and is also the frequency of the model wave.

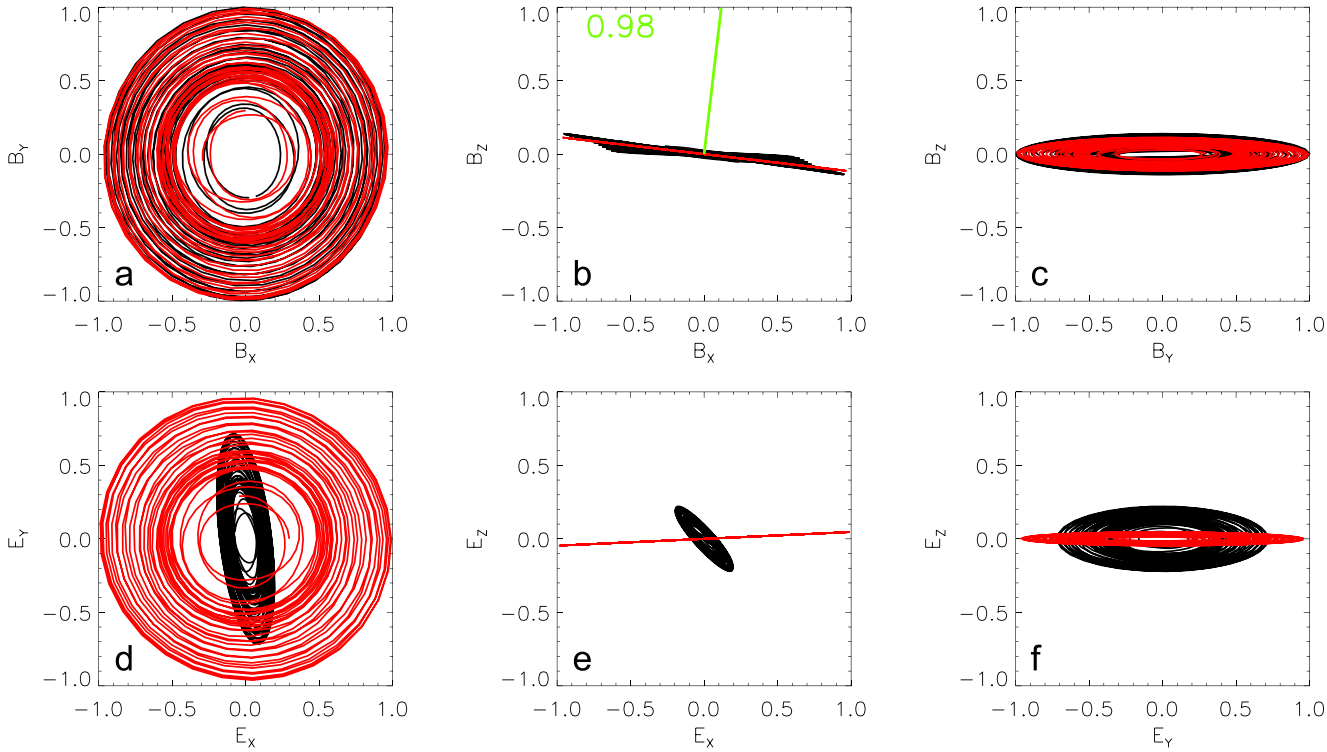

Figure 7. The observed (black) and modeled (red) whistler-mode wave in XYZ coordinates.

The result is a modeled waveform, and an observed waveform, which can be directly compared. The modeled waveform can be compared to the observed waveform before any sheath correction is applied, as well as after the sheath correction has been applied to each electric field component. This directly tests the impact of applying the sheath model to the electric field waveform data.

Figure 7 shows the measured (black) and modeled (red) waveforms of B in the (a) x-y plane, (b) x-z plane, and (c) y-z plane. The electric field is shown in panels (d–f). For the magnetic field, there is a clear consistency in the between data and model. The straight line observed in the x-z plane (Figure 7b) for the modeled wave is as expected for a plane wave with the k vector confined to the x-z plane. The fact that the observed wave (black line) does not stray too far from this plane indicates a high degree of planarity (0.98 in this case). The green line indicates the orientation of the k vector (perpendicular to the plane of polarization). For the electric field there is a clear disagreement between data and model, with large differences primarily apparent in the E_x and E_z directions, and smaller deviations apparent in E_y.

To identify if these deviations are primarily caused by one measurement direction, these plots are reproduced in the U, V, W boom/sensor coordinate system. Figure 8 shows the measured (black) and modeled (red) waveforms of B in the (a) u-v plane, (b) u-w plane, and (c) v-w plane. Again, the electric field is shown in panels (d–f). For the magnetic field, the observations and model are largely in agreement. For the electric field, it is apparent that the primary source of differences between the data and the model can be attributed to E_w, with the observed electric field amplitude along this direction being only a small fraction (10% or less) of that predicted by the model. Smaller deviations between the data and model are observed in E_u and E_v, with the observed amplitudes being around 80% of the modeled values. Note that in this format it is not possible to identify phase differences between the observed and modeled waves.

Figure 9 shows the time series of the measured (black) and modeled (red) magnetic field waveforms; (a) B_u, (b) B_v, and (c) B_w. The electric field waveforms prior to the sheath correction being applied are shown in (d) E_u, (e) E_v, and (f) E_w. The electric field waveforms after the sheath correction has been applied are shown in (g) E_u^{cor}, (h) E_v^{cor}, and (i) E_w^{cor}. Instantaneous amplitudes of each component are shown by dotted lines. When

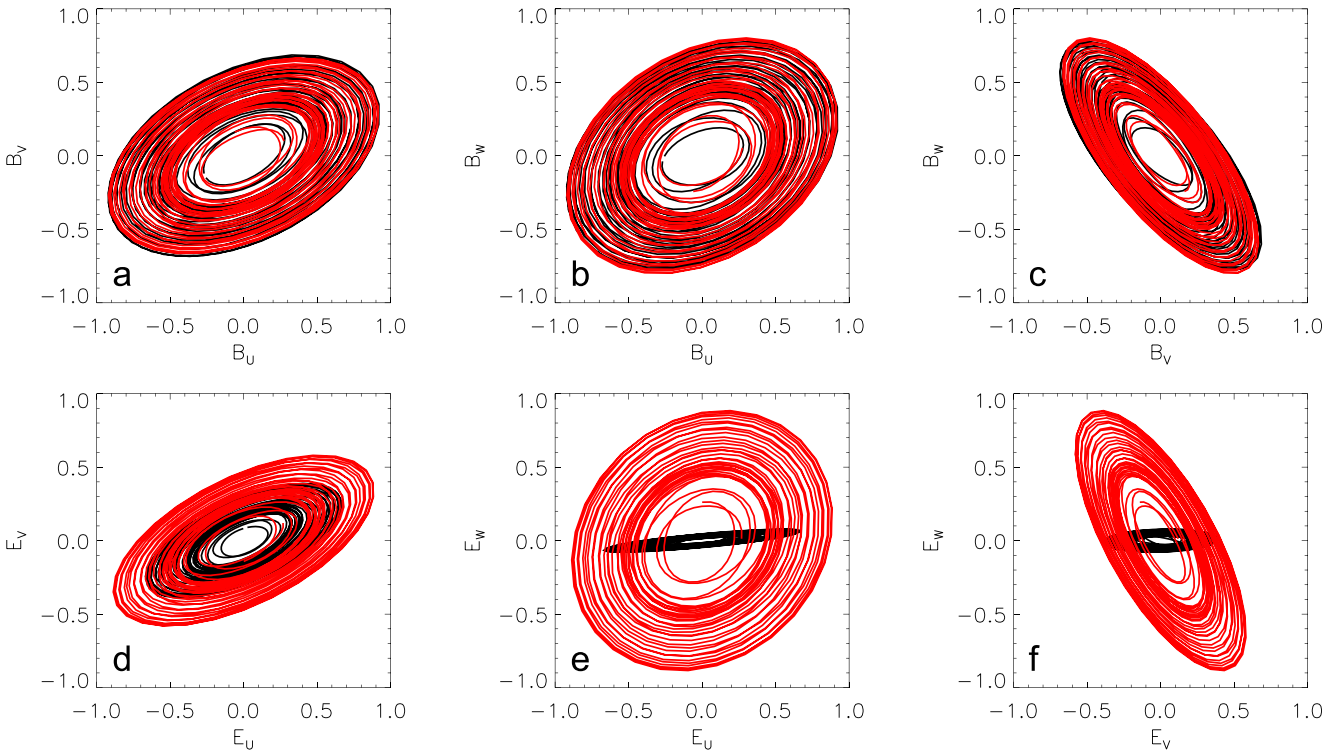

Figure 8. The observed (black) and modeled (red) whistler-mode wave in UVW coordinates.

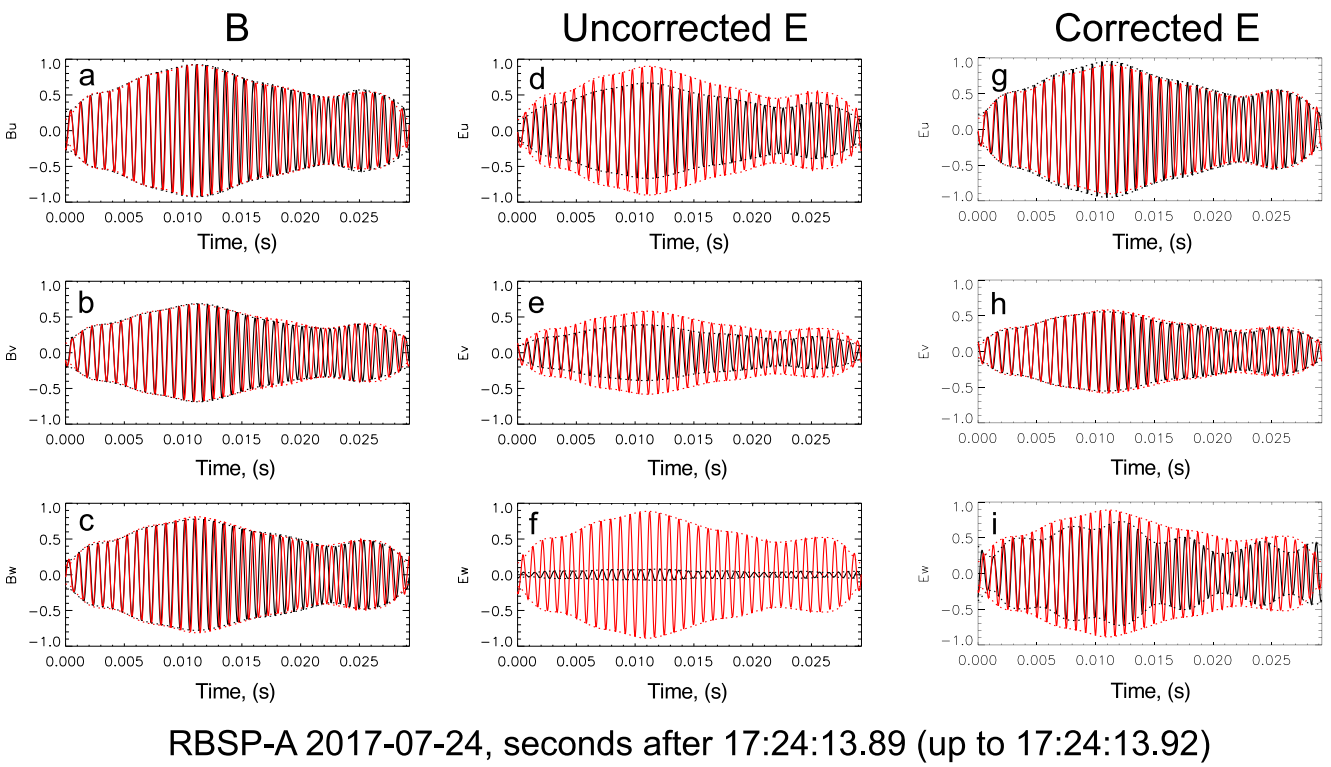

Figure 9. Time series of the observed (black) and modeled (red) wave in UVW coordinates, both before (d, e, f) and after (g, h, i) the sheath correction has been applied to the measured electric field. Instantaneous amplitudes of each component are shown by dotted lines.

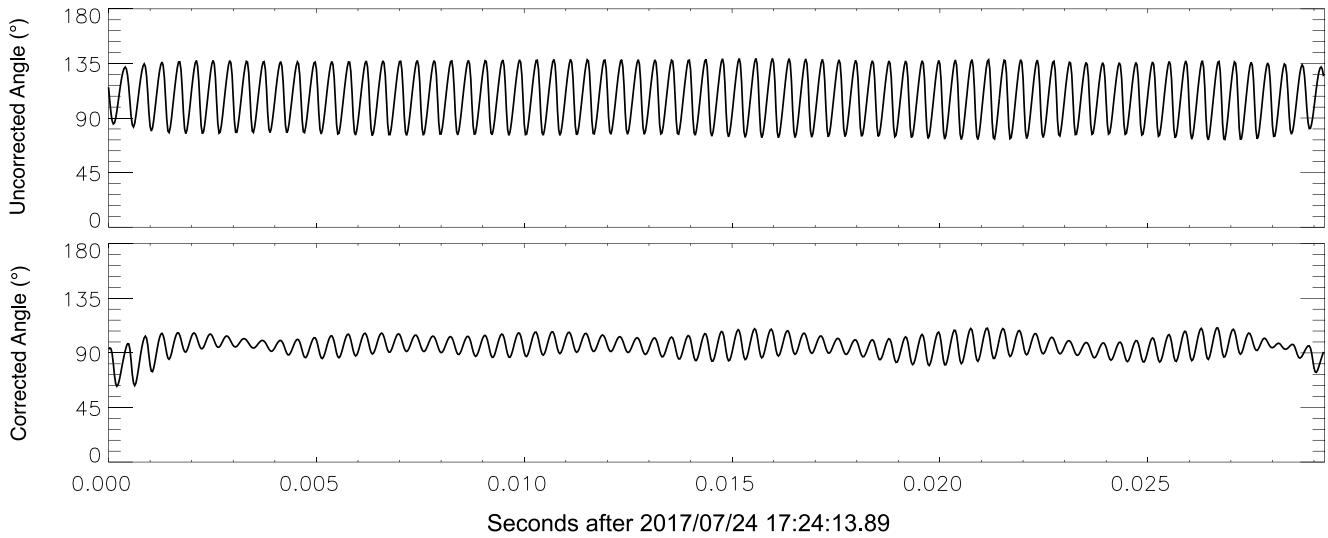

Figure 10. Time series of the angle (°) between E and B vectors before (top) and after (bottom) the sheath correction has been applied.

the magnetic field wave amplitude is largest, the magnetic field data and model are in agreement in both phase and amplitude. At other time periods, the B amplitudes are in agreement but the phase is not. This is attributed to the fixed frequency used in the model, whereas frequency variations may exist in the observations due to the rising tone nature of the chorus element, as well as its subpacket structure. For the uncorrected electric field, the observed wave amplitude of E_u and E_v is only around 80% of the modeled wave, whereas the amplitude of E_w is only around 10% of that modeled. Once the sheath correction has been applied, the amplitude of E_u^{cor}, E_v^{cor}, and E_w^{cor} are all closer to the modeled wave. The amplitude of E_u^{cor}, E_v^{cor} are in very close agreement with the modeled wave, whereas the amplitude of E_w^{cor} remains slightly less than the modeled wave, but is significantly closer to the modeled wave than the uncorrected value.

The phase differences between the modeled and observed electric field are also determined by calculating the phase of the complex amplitude ratio between data and model. In this case, prior to the sheath correction being applied, E_u has a phase difference of $-13°$, E_v has a phase difference of $-10°$, and E_w has a phase difference of $-60°$. After the sheath correction has been applied to the observations, the phase differences between data and model are $-5°$ for E_u, $-2°$ for E_v, and $-3°$ for E_w. This represents a substantial increase in agreement between the data and the modeled wave.

To further test the impact of the sheath correction, the angle between the **E** and **B** vectors is considered (where **E** and **B** refer to the electric and magnetic field associated with the whistler mode wave, $\mathbf{E}_{wave}$ and $\mathbf{B}_{wave}$, and not the background magnetic field, $\mathbf{B}_0$). A consequence of Faraday's Law is that $\mathbf{E} \cdot \mathbf{B} = 0$, or that the **E** and **B** vectors are perpendicular, with the angle between them being 90°. This is most easily visualized for parallel propagating waves, where $\mathbf{E}_{wave}$ and $\mathbf{B}_{wave}$ remain in the plane perpendicular to $\mathbf{B}_0$. However, following from the Fourier transform of the Faraday's law, the relationship remains true for all plane waves regardless of the k-vector direction, even for oblique cases where $\mathbf{E}_{wave}$ may have a component along $\mathbf{B}_0$ (e.g., Cattell et al., 2008; Mozer et al., 2014). Figure 10 shows the angle between $\mathbf{E}_{wave}$ and $\mathbf{B}_{wave}$ in the time domain both before (top) and after (bottom) the sheath correction has been applied. Prior to applying the sheath correction, the angle between E and B oscillates primarily between ∼70 and 140°. After applying the sheath correction, the angle is much closer to 90°, and the magnitude of the oscillation is substantially reduced. In this test case it is evident that applying the sheath correction brings the observations more in line with what would be expected from Faraday's Law, albeit not completely removing the oscillatory behavior.

This analysis is subsequently applied to a longer time period, encompassing the entire chorus element as it sweeps through a range of frequencies, thus allowing the sheath correction to be tested over a broader frequency range. Time periods are only considered if the total magnetic field wave power exceeds 10^{-7} nT^2/Hz and the planarity exceeds 0.90. We note that due to frequency averaging, and the number of spectral matrices in each frequency bin,

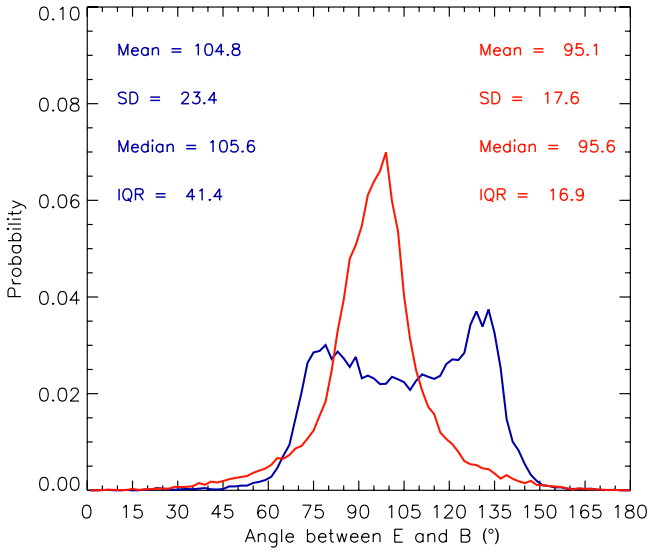

Figure 11. Histogram of the angle (°) between E and B vectors before (blue) and after (red) the sheath correction has been applied.

a stricter planarity threshold is often required for burst mode data as opposed to survey mode data. We also note here that the limitation that $\theta_k < 15°$ used when building the model, is no longer implemented during model testing. Figure 11 shows a histogram of the angle between E and B throughout this period, with pre-correction values shown in blue and post-correction values shown in red. The distribution parameters prior to the sheath correction being applied are; Mean = 104.8°, Standard Deviation = 23.4°, Median = 105.6°, Interquartile Range = 41.4°. These same parameters for the sheath corrected distribution are; Mean = 95.1°, Standard Deviation = 17.6°, Median = 95.6°, Interquartile Range = 16.9°. These statistics demonstrate that the sheath correction brings the average angle between E and B closer to 90°, as well as substantially reducing the spread of values from the average. As such, it is evident that applying the sheath correction results in the angle between E and B converging closer to 90°, in closer agreement with Faraday's Law.

Applying this technique to different whistler-mode waves, both chorus and lightning generated whistlers, which occur in different plasma environments allows for the sheath correction to be tested over a broad range of plasma densities. Figure 12 shows the impact of the sheath correction for several time intervals where whistler-mode waves are observed. Different minimum threshold values are implemented for the total magnetic field wave power for each event, due to the varying background signals between events. The minimum planarity (Santolík et al., 2003) threshold imposed in each of the events is 0.90. The left panels show spectrograms of the magnetic field wave power and the right panels show histograms of the angle between E and B both before (blue) and after (red) the sheath correction has been applied.

Interval 1 is a lightning generated whistler observed by RBSP-B on 2016-08-02 at $L = 2.57$, starting at 14:04:05.4 and lasting 1 second, between 200 and 5,000 Hz and where the plasma density is 1,050 cm^{-3}. The total magnetic field wave power at each time interval must exceed 10^{-6} nT^2/Hz. For this event, the distribution of angles between E and B has the following parameters prior to the sheath correction being applied; Mean = 74.5°, Standard Deviation (SD) = 19.4°, Median = 78.0°, Interquartile Range (IQR) = 20.4°. These same parameters for the sheath corrected distribution are; Mean = 87.0°, Standard Deviation = 14.7°, Median = 88.2°, Interquartile Range = 10.2°.

Interval 2 contains a series of chorus elements observed by RBSP-A at $L = 5.55$ occurring on 2012-11-14 between 13:44:40 and 13:44:47. The frequency of these chorus elements is between 400 and 1,700 Hz, the plasma density during this interval is 5 cm^{-3}, and the total magnetic field wave power must exceed 10^{-4} nT^2/Hz to be included in the analysis. For this event, the distribution of angles between E and B has the following parameters prior to the sheath correction being applied; Mean = 76.7°, Standard Deviation = 31.4°, Median = 75.8°, Interquartile Range = 55.3°. These same parameters for the sheath corrected distribution are; Mean = 88.7°, Standard Deviation = 13.2°, Median = 88.7°, Interquartile Range = 16.5°.

Interval 3 is another lightning generated whistler observed by RBSP-A occurring on 2016-08-20 starting at 14:18:58.7 and lasting 0.5 seconds. The wave frequency is between 200 Hz and 12 kHz, the plasma density is 1,150 cm^{-3}, the spacecraft is located at $L = 2.45$, and the total magnetic field wave power threshold implemented in this case is 10^{-6} nT^2/Hz. For this event, the distribution of angles between E and B has the following parameters prior to the sheath correction being applied; Mean = 69.6°, Standard Deviation = 27.4°, Median = 68.2°, Interquartile Range = 38.4°. These same parameters for the sheath corrected distribution are; Mean = 83.2°, Standard Deviation = 19.9°, Median = 83.1°, Interquartile Range = 10.0°.

In all three cases, the post-sheath-correction values exhibit a greater level of agreement with Faraday's law, with the mean and median angle between E and B being closer to 90°, as well as the spread of values from this average being substantially reduced, as indicated by both the standard deviation and the interquartile range.

This sheath correction has been applied to the full Van Allen Probes mission to produce a full sheath corrected EMFISIS L4 data set. Further details of this data set are provided in Section 5. To statistically demonstrate the

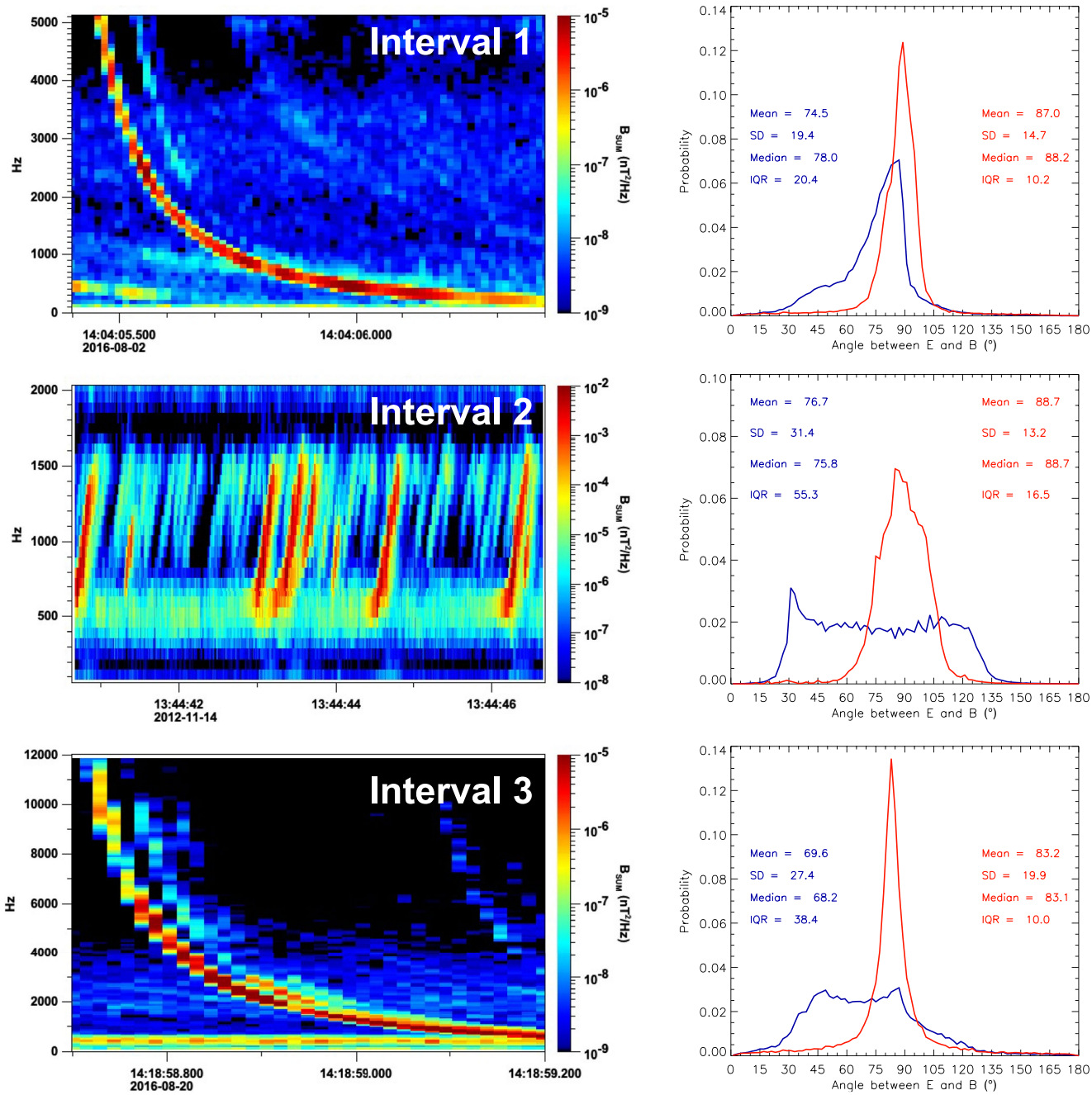

Figure 12. (left) Power spectral density of the magnetic field for three different periods of whistler-mode waves and (right) histograms of the angle (°) between E and B vectors before (blue) and after (red) the sheath correction has been applied.

effectiveness of the sheath correction, this full data set from both spacecraft is used to determine the angle between E and B for all waves which meet the following criteria; (a) the total magnetic field wave power exceeds 10^{-7} nT^2/Hz; (b) the degree of magnetic field ellipticity (Santolík et al., 2002) and polarization (Santolík & Gurnett, 2002) of the magnetic field polarization exceed 0.5; (c) the planarity (Santolík et al., 2003) of the magnetic field polarization exceeds 0.8; (d) the wave frequency is greater than 30 Hz and; (e) density data are available and can therefore be used to determine the sheath correction. These selection criteria isolate whistler-mode waves with right hand circular polarization, are approximately planar, and have significant wave amplitude. Note that a

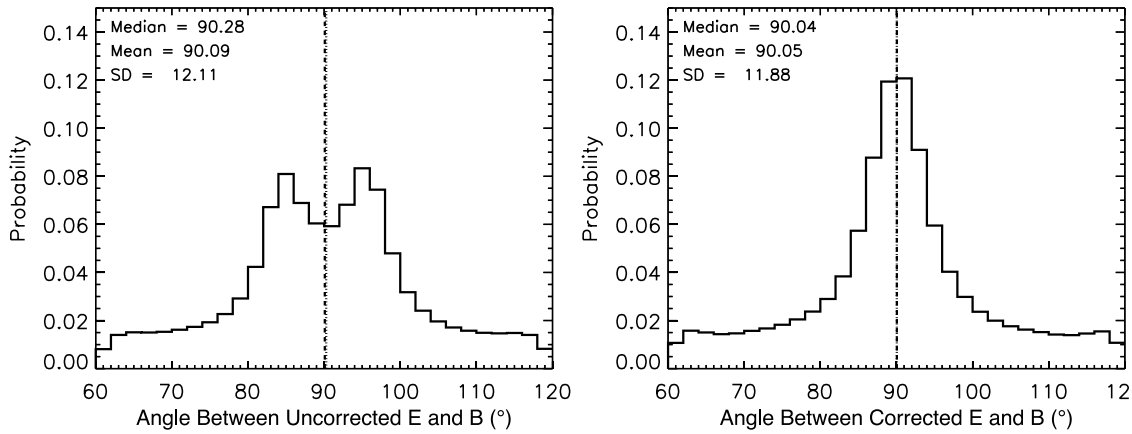

Figure 13. Histograms of the angle between E and B (°) determined in the frequency domain for the full RBSP mission before (left) and after (right) the sheath correction has been applied.

stricter selection criteria is imposed here when testing the correction to ensure the validity of the testing metrics (e.g., $\mathbf{E}_{wave} \cdot \mathbf{B}_{wave} = 0$).

The angle between E and B is determined from the spectral matrices as described in Appendix E. Having determined the angle between E and B both before and after the sheath correction has been applied, the results are compared to the expectation of 90° from Faraday's Law. Figure 13 contains histograms of the angle between E and B before (left) and after (right) the sheath correction has been applied to the data. The vertical dashed line is the mean value and the vertical dotted line is the median. Prior to the sheath correction being applied to the data, a double peaked distribution is observed, with a local minima at the expected value of 90°. The median of the distribution is 90.28, the mean is 90.09. After the sheath correction has been applied, a single peak is observed in the distribution centered on 90°, in agreement with Faraday's Law. The median of the sheath corrected distribution is 90.04 and the mean is 90.05.

The bifurcated distribution apparent prior to the sheath correction being applied is due to oppositely directed Poynting vectors. For Poynting vectors which contain a component that is parallel to the background magnetic field, that is, the polar angle of Poynting vector, θ_S, is less than 90°, the sheath effects cause the observed angle between E and B to be less than 90°. For Poynting vectors which contain a component that is anti-parallel to the background magnetic field with θ_S being greater than 90°, the sheath effects cause the observed angle between E and B to be greater than 90°. This is demonstrated in Figure 14, which contains histograms of the angle between E and B for (top) polar angle of Poynting vector is less than 90°, (bottom) polar angle of Poynting vector is greater than 90°, (left) prior to sheath correction being applied, and (right) after the sheath correction has been applied. Again, the vertical dashed (dotted) line is the mean (median) value.

For θ_S less than 90° and prior to the sheath correction being applied, the distribution is clearly peaked with the angle between E and B typically greater than 90° with the median being 94.32° and the mean being 92.50°. After the sheath correction is applied, these values become a median of 90.45° and a mean of 90.01°. A similar picture is true for θ_S greater than 90°. Prior to the sheath correction being applied, the distribution is clearly peaked below 90° with the median being 86.04° and the mean being 87.72°. After the sheath correction is applied, these values become a median of 89.65° and a mean of 89.91°. In both cases, field-aligned and anti-field-aligned Poynting vector directions, the sheath correction shifts the distribution to be closer to the expected result of 90°.

Figure 15 contains a schematic explaining how the direction of the Poynting vector, S, bifurcates the distribution in the angle between E and B due to phase shifts in the electric field. In the simple case shown in the top left where the real wave has perpendicular E and B, with S, k, and B_0 coming out of the page. We then apply a clockwise phase shift to E (due to sheath effects), which changes the phase of E such that the angle between E and B is larger than 90° as shown in the top right. If we then consider the same wave, but propagating with k and S into the page, we have the setup shown on the bottom left. Applying the same clockwise phase shift to E, since

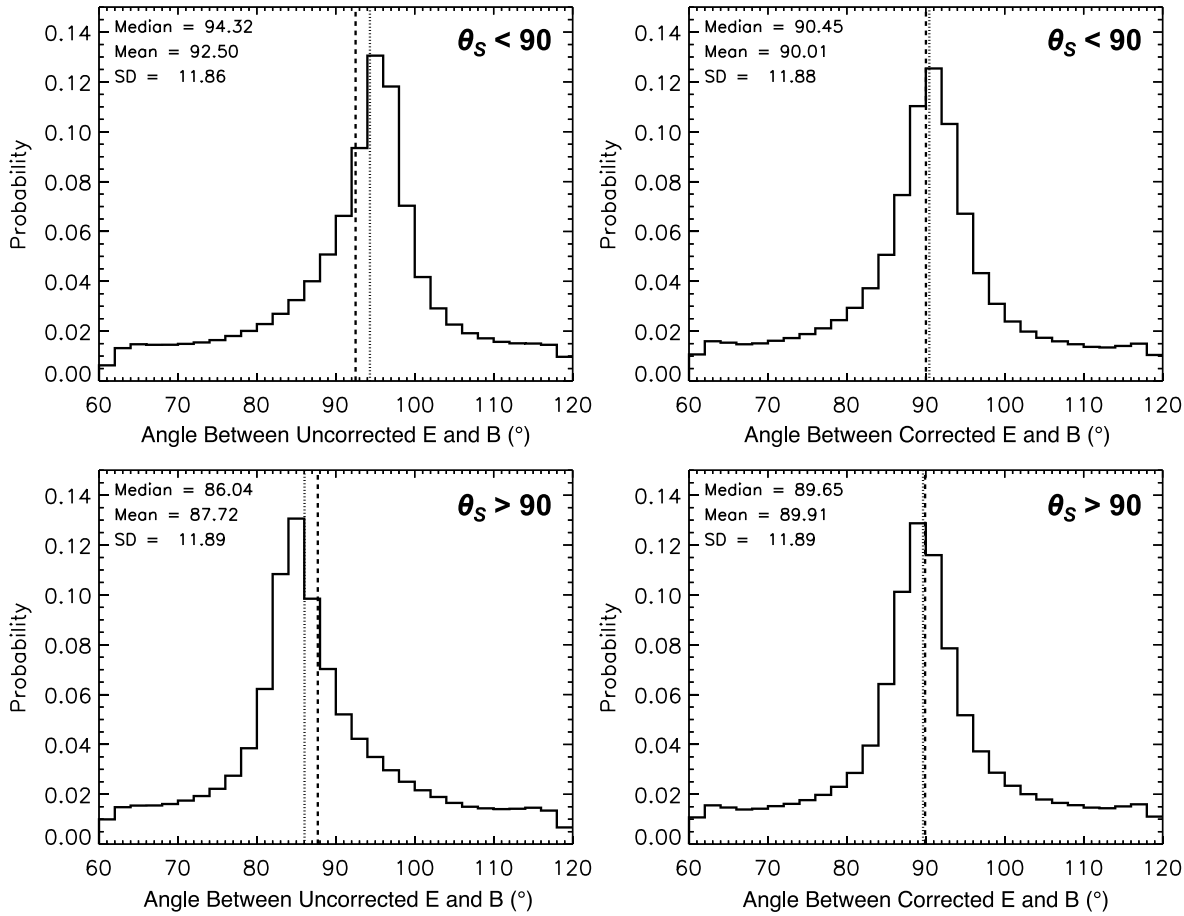

Figure 14. Histograms of the angle between E and B (°) determined in the frequency domain sorted by parallel (top) and anti-parallel (bottom) Poynting vector direction both before (left) and after (right) the sheath correction has been applied.

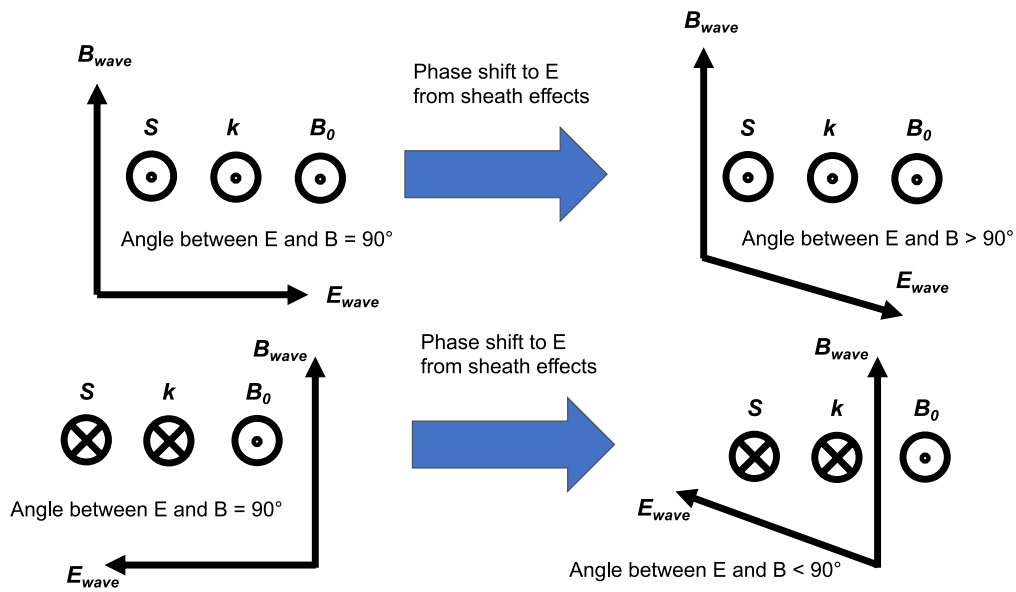

Figure 15. Schematic showing how the angle between *E* and *B* shifts in opposite directions away from 90° depending on the Poynting vector direction when a phase shift due to sheath effects is applied to *E*.

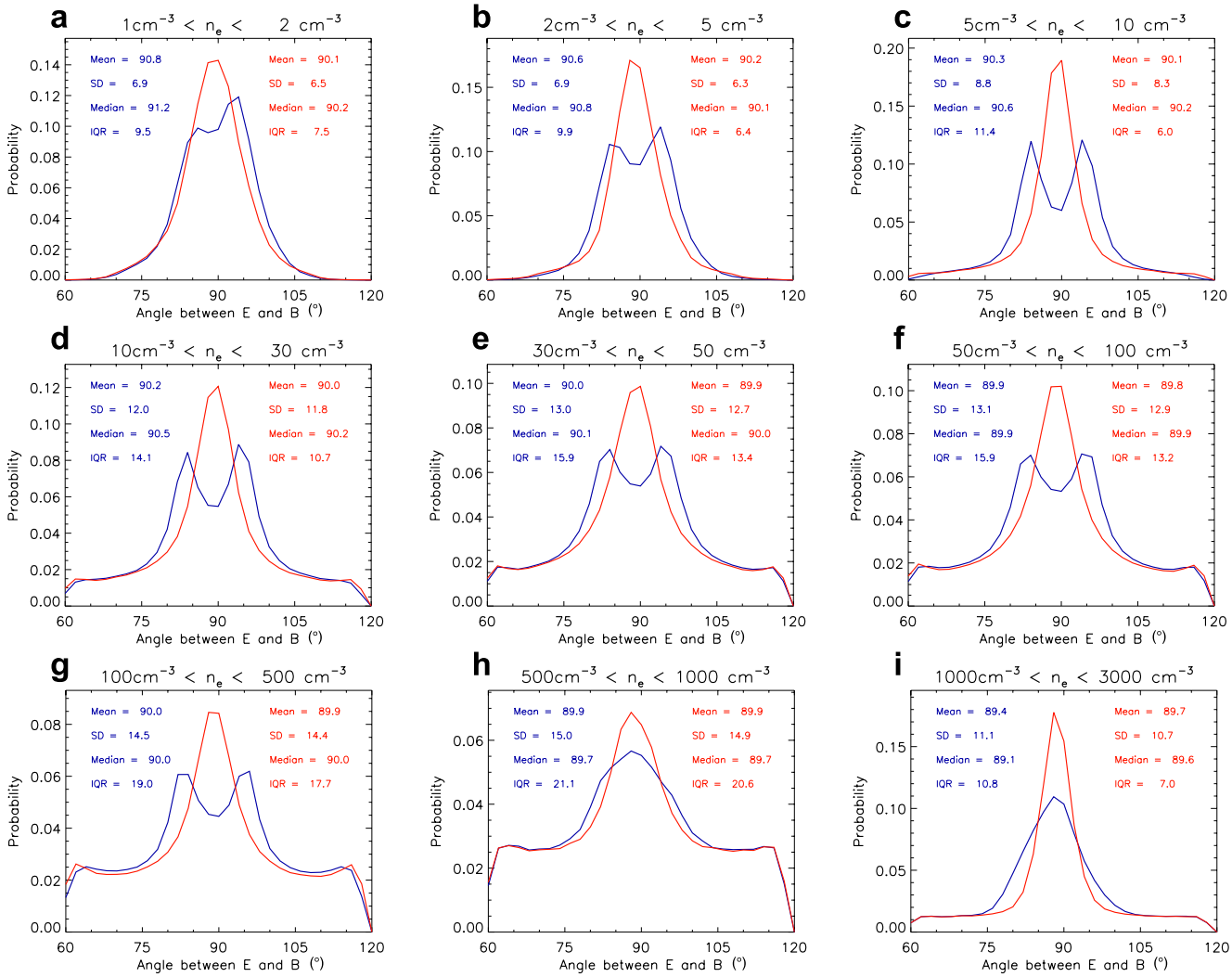

Figure 16. Histograms of both the uncorrected (blue) and corrected (red) angle between E and B (°) determined in the frequency domain for a range of different plasma densities.

the antenna geometry is independent of the wave propagation direction, we get the resulting measurement shown in the bottom right, with the angle between E and B being less than 90°. This is exactly the result obtained with real data in Figure 14. That is, k parallel to B_0 (e.g., $\theta_S < 90°$) we get the angle between E and B being larger than 90°, and for k anti-parallel to B_0 (e.g., $\theta_S > 90°$) we get the angle between E and B being smaller than 90°. This bifurcated distribution is reconciled into a single peak by the sheath correction, centered on agreement with Faraday's Law.

Figure 16 shows the impact of the sheath correction on the angle between E and B for a range of different plasma densities. Data are shown for all Poynting vector directions, with pre-correction values shown in blue and sheath-corrected data shown in red. The bifurcated distribution in the pre-correction values is once again apparent. Data are shown for plasma densities of; (a) 1 cm^{-3} < n_e < 2 cm^{-3}; (b) 2 cm^{-3} < n_e < 5 cm^{-3}; (c) 5 cm^{-3} < n_e < 10 cm^{-3}; (d) 10 cm^{-3} < n_e < 30 cm^{-3}; (e) 30 cm^{-3} < n_e < 50 cm^{-3}; (f) 50 cm^{-3} < n_e < 100 cm^{-3}; (g) 100 cm^{-3} < n_e < 500 cm^{-3}; (h) 500 cm^{-3} < n_e < 1,000 cm^{-3} and; (a) 1,000 cm^{-3} < n_e < 3,000 cm^{-3}. In all cases the sheath correction causes a more pronounced peak to the distribution that is centered closer to the expected value of 90°, and reduces the spread of the distribution.

Overall, these tests have conclusively shown that applying the sheath correction to the electric field observations brings them more in line with what is expected from theory, both using waveform data in the time domain and using spectral data in the frequency domain.

5. Sheath Corrected Data Set

This sheath correction has been applied to the full Van Allen Probes mission to produce a full sheath corrected EMFISIS L4 data set. This data set contains what we believe are the most accurate wave electric field measurements currently derivable from the Van Allen Probes mission. In addition, higher order data products which derive from electric field observations such as, but not limited to, spectral estimates of the Poynting vector magnitude and direction (e.g., Santolík et al., 2010), are also affected by the sheath correction. These updated values are also contained within the sheath corrected data set. It is hoped that the steps taken in this study will improve clarity in observations and result in a more accurate understanding of electromagnetic waves in the terrestrial magnetosphere, their interactions with different particle populations, and the propagation and energy flow of these waves.

Appendix A: Recover Complex Amplitude From Spectral Matrices

Consider an ideal, monochromatic plane wave of frequency ω, with a k-vector along the z-axis. The vector electric field $\vec{\mathbf{E}}$ can be represented as;

$$\vec{\mathbf{E}} = (E_x\hat{\mathbf{x}} + E_y\hat{\mathbf{y}})\, e^{-i(\omega t - kz)}, \tag{A1}$$

where E_x and E_y are the complex amplitudes of the two components of the electric field vector in the plane of the wave. If this were instead a representation of a single frequency within the spectral domain of a more general wave, then E_x and E_y would be the complex coefficients of the FFT for frequency ω. Each complex amplitude can be further expressed as a real amplitude with a phase, giving

$$\vec{\mathbf{E}} = \left(\tilde{E}_x e^{i\alpha}\hat{\mathbf{x}} + \tilde{E}_y e^{i\beta}\hat{\mathbf{y}}\right) e^{-i(\omega t - kz)}. \tag{A2}$$

Thus, it is the phases α and β, and the real amplitudes $\tilde{E}_x$ and $\tilde{E}_y$, that determine the orientation and time evolution of the E-vector in the x-y plane–i.e. the polarization of the vector. The phase of the B-vector is tied to that of the E-vector via Maxwell's equations.

It is important to note that in many contexts, it is only the phase differences (e.g., $\alpha - \beta$, in our simplified case) between the components of the vectors that are important. For instance, these values are what differentiates between linear, circular, or elliptical polarization. In the case of a Fourier representation of a complex waveform, it is further the case that the relative phases between the different frequency coefficients (for a given signal) are key to how the various Fourier terms add to create the net waveform.

For the Van Allen Probes survey data, measurements of the electric and magnetic fields are available only in the form of spectral matrices. These are constructed on board the spacecraft using 0.468 s of waveform data, collected every ∼6 s. The elements of each spectral matrix consist of a combination of the auto-correlations (e.g., $B_x B_x^*$) of the Fourier coefficients for each available waveform, plus the cross-correlations (e.g., $B_x E_y^*$) of the coefficients of each non-matching pair of signals. These spectral matrices are then summed over variably-sized frequency bins (with logarithmic spacing), before being sent to the ground.

When constructing and testing the sheath correction algorithm, it is necessary to recover both the magnitude and phase of the original individual waveforms, at least in the frequency-binned sense that is available. To illustrate this recovery process, consider our case where three electric and three magnetic orthogonal components have been used to construct a 6 x 6 spectral matrix. The real magnitudes of the six field components are easily reconstructed from the square root of the diagonal elements ($B_x B_x^*$, $B_y B_y^*$, $B_z B_z^*$, $E_x E_x^*$, $E_y E_y^*$ and $E_z E_z^*$). The absolute phases of the six fields are generally not recoverable, but as noted above, the relative phases are often the physically interesting quantities, and these can be reconstructed by using the unique off-diagonal elements

$$
\begin{array}{ccccc}
B_x B_y^* & B_x B_z^* & B_x E_x^* & B_x E_y^* & B_x E_z^* \\
 & B_y B_z^* & B_y E_x^* & B_y E_y^* & B_y E_z^* \\
 & & B_z E_x^* & B_z E_y^* & B_z E_z^*. \\
 & & & E_x E_y^* & E_x E_z^* \\
 & & & & E_y E_z^*
\end{array}
$$

Let F and G each represent one of the complex amplitudes B_x, B_y, B_z, E_x, E_y or E_z, and be expressed in terms of real amplitudes ($\tilde{F}$, $\tilde{G}$) and phases (f, g)

$$F = \tilde{F} e^{if} \tag{A3}$$

$$G = \tilde{G} e^{ig}. \tag{A4}$$

A spectral matrix cross-term FG^* would therefore be

$$FG^* = \tilde{F}\tilde{G} e^{i(f-g)} \tag{A5}$$

from which it is apparent that the phase of each cross-term is just the difference in the phases of its components

$$\text{phase}\,(FG^*) \equiv \Phi\,(FG^*) = \Phi(F) - \Phi(G). \tag{A6}$$

Examining the available spectral matrix cross terms, we see that they can be combined in multiple ways to produce any given phase difference. For example, there are five ways to construct the $B_y - B_x$ phase difference:

$$
\begin{aligned}
\Phi\,(B_y) - \Phi\,(B_x) &= -\arctan\left(\frac{\Im\left(B_x B_y^*\right)}{\Re\left(B_x B_y^*\right)}\right) \\
&= \arctan\left(\frac{\Im\,(B_y B_z^*)}{\Re\,(B_y B_z^*)}\right) - \arctan\left(\frac{\Im\,(B_x B_z^*)}{\Re\,(B_x B_z^*)}\right) \\
&= \arctan\left(\frac{\Im\,(B_y E_x^*)}{\Re\,(B_y E_x^*)}\right) - \arctan\left(\frac{\Im\,(B_x E_x^*)}{\Re\,(B_x E_x^*)}\right) \\
&= \arctan\left(\frac{\Im\left(B_y E_y^*\right)}{\Re\left(B_y E_y^*\right)}\right) - \arctan\left(\frac{\Im\left(B_x E_y^*\right)}{\Re\left(B_x E_y^*\right)}\right) \\
&= \arctan\left(\frac{\Im\,(B_y E_z^*)}{\Re\,(B_y E_z^*)}\right) - \arctan\left(\frac{\Im\,(B_x E_z^*)}{\Re\,(B_x E_z^*)}\right).
\end{aligned} \tag{A7}
$$

where we have used Euler's formula to note that any complex value C is related to its phase c via

$$\frac{\Im C}{\Re C} = \tan(c). \tag{A8}$$

Similarly, there are five distinct ways to calculate the phase of each of the remaining four field components relative to B_x. To obtain a final estimate for each of these five phase differences, a simple average of each set of five distinct values is used.

Appendix B: Table of Sheath Model Coefficients

The following table summarizes the sheath impedance model coefficients as a function of plasma density for the spin-plane. $C_L = 7$ pF and $R_L = 1$ TΩ.

n_e (cm^{-3})	R_S (MΩ)	C_S (pF)	s_f	λ_S (°)
0.1	900	1.00	1.00	0.00
0.2	900	1.00	1.00	0.00
0.5	759	2.09	1.00	0.00
1	298	5.25	1.00	0.00
2	99.6	9.11	1.00	0.00
5	25.6	13.2	1.00	0.00
10	12.5	16.5	1.00	0.00
20	8.94	18.4	1.00	0.00
50	5.86	19.6	1.00	0.00
100	3.97	20.3	1.00	0.00
200	2.80	20.9	1.00	0.00
500	1.51	21.6	1.00	0.00
1,000	1.28	22.0	1.00	0.00
2,000	1.21	22.0	1.00	0.00

The following table summarizes the sheath impedance model coefficients as a function of plasma density for the spin-axis. $C_L = 6$ pF and $R_L = 1$ TΩ.

n_e (cm^{-3})	R_S (MΩ)	C_S (pF)	s_f	λ_S (°)
0.1	1,060	0.117	0.600	0.00
0.2	817	0.137	0.707	0.00
0.5	579	0.170	0.849	0.00
1	447	0.200	0.956	0.00
2	344	0.234	1.00	0.00
5	244	0.290	1.00	2.07
10	188	0.341	1.08	9.75
20	145	0.401	1.29	17.8
50	103	0.496	1.49	26.5
100	79.4	0.583	1.60	30.0
200	61.3	0.686	1.56	27.2
500	43.4	0.849	1.21	18.5
1,000	33.5	0.998	1.08	11.0
2,000	25.8	1.17	1.03	2.07

Appendix C: Instrument Noise Floor

It is important that the sheath corrections not be applied to any electric field data that are at, or below, the noise floor of each measurement direction. Applying corrections to such signals could incorrectly amplify these noise levels. The first step in establishing this noise floor is to survey the data set for a selection of intervals where the electric field data are very quiet. The result of this survey is a set of manually-selected intervals which show only instrument-noise signal levels, if not for the full frequency range, then at least for subsets of it. These intervals vary in length from a few minutes to a few tens of minutes, and span both spacecraft and almost the whole extent of the mission.

Next, each interval is analyzed to generate a histogram for each frequency bin, using all the spectral density values observed at that frequency during the interval. For an ideal quiet interval (i.e., no non-noise signal), each of these observations would be a sampling from the pure noise distribution. Assuming a roughly Gaussian distribution, the median, mean, and peak should be approximately equal. We use the median as the single value to represent this distribution, as it is the least susceptible to scatter amongst the measured values.

For a more typical interval, there will be some non-noise signal in the observed distribution at any given frequency. Since all such signals will be at spectral density values equal to, or higher than, the noise level, such signals can only increase the median of the observed distribution. Thus, upon examining all the intervals, the distribution with the lowest median should be the one least influence by non-noise signals, and so is selected as representative of the noise floor. This assessment is done for each frequency independently, and the set comprising each of these lowest median values is then identified as the first draft of the frequency-dependent noise floor. By doing so, we make use of the piece-wise (in frequency) quiet nature of the intervals.

The electric field data are also inspected for any systematic temporal trends over the lifetime of the mission. The presence of any significant trend would require the construction of an epoch-dependent noise floor, but that is not seen to be the case here. Therefore, the noise floors are considered to be constant over the lifetime of the mission. Note that this is not the case for the noise floor of the magnetic search coil antennas, discussion of which is beyond the scope of this paper. Examining the draft floors for the two spin-plane electric booms/sensors (U and V), it is evident that, as expected, they are very similar. Thus, their two floors are compared, with the lowest of the two values at each frequency taken to be the combined spin-plane noise floor, using the same reasoning as in the previous paragraph. Finally, a 3-point median filter is applied to the two draft noise floors (one for spin axis and one for spin plane). This smooths some of the remaining statistical fluctuations, and removes the effect of the narrow-band interference noise lines seen at certain fixed frequencies. Since data at these frequencies are generally unusable, it is deemed a justifiable simplification to ignore the effect of the noise lines when applying sheath corrections.

Figure 17 illustrates this process for the three boom/sensor directions on RBSP-A. The different colored solid lines show the median spectral density values for each of the quiet intervals examined, while the dashed black line shows the minimum value at each frequency, after the median filter has been applied. For the spin-plane (Figures 17a and 17b), these black lines are identical, showing the combined spin-plane noise floor.

The above process is undertaken individually for each spacecraft, with the resulting two pairs of noise floors subsequently compared. The variations seen between spacecraft, for each type of noise floor, are of comparable magnitude to those seen within the floors for either spacecraft individually, so simple averages over the two spacecraft are taken, with the output being the final spin axis and spin plane noise floors.

In practice, using these noise floors directly as the threshold for applying the sheath corrections is found to result in false artifacts in the processed data, as signals at, or very near to, the noise floor can become excessively enhanced. To mitigate this, a case study analysis is performed, wherein multiple datasets are generated by applying the sheath corrections using different thresholds, each a different scalar multiple of the noise floor. Spectrograms are then generated for each of these datasets, and compared to the uncorrected data, with the goal of determining which case best preserves the qualitative appearance of the uncorrected spectra, and minimizes visual artifacts at low signal levels. The appearance of the spectra near density changes (which can have a large effect on the size of the sheath correction) is particularly sensitive to this scaling factor. An example of this analysis for the E_w direction on RBSP-A is shown in Figure 18 for (a) the uncorrected data, (b) a scaling factor of ten, and (c) a scaling factor of one. In Figure 18c, artifacts caused by abrupt density changes, as seen in Figure 18d,

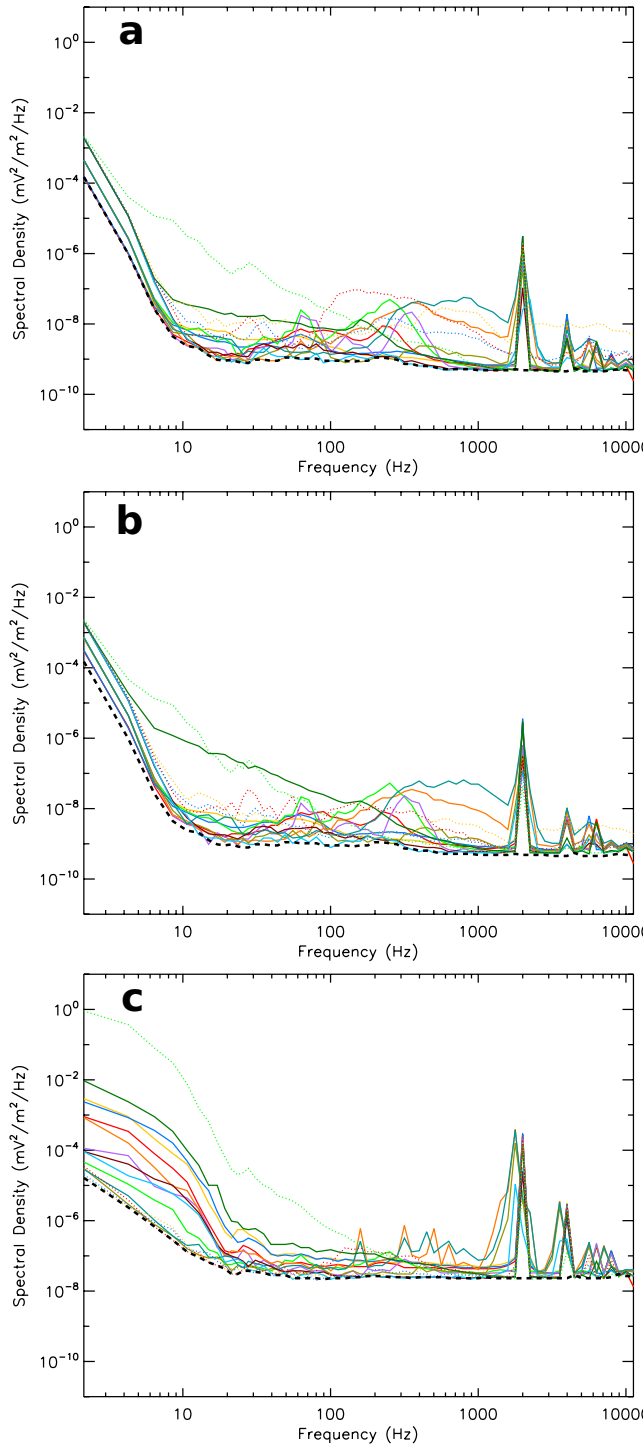

Figure 17. Construction of electric field noise floors for the (a) E_u, (b) E_v and (c) E_w directions on RBSP-A.

can clearly be seen in the irregular vertical banding of the low-level signal between 06:15 and 07:30. We find that the best results are observed when each of the noise floors is multiplied by a factor of ten before being used as the sheath correction threshold.

One technical detail that this noise floor analysis has not yet addressed is the selectable attenuation of the electric field data. The EFW instrument contains a 19 dB attenuation circuit that can be commanded into either an

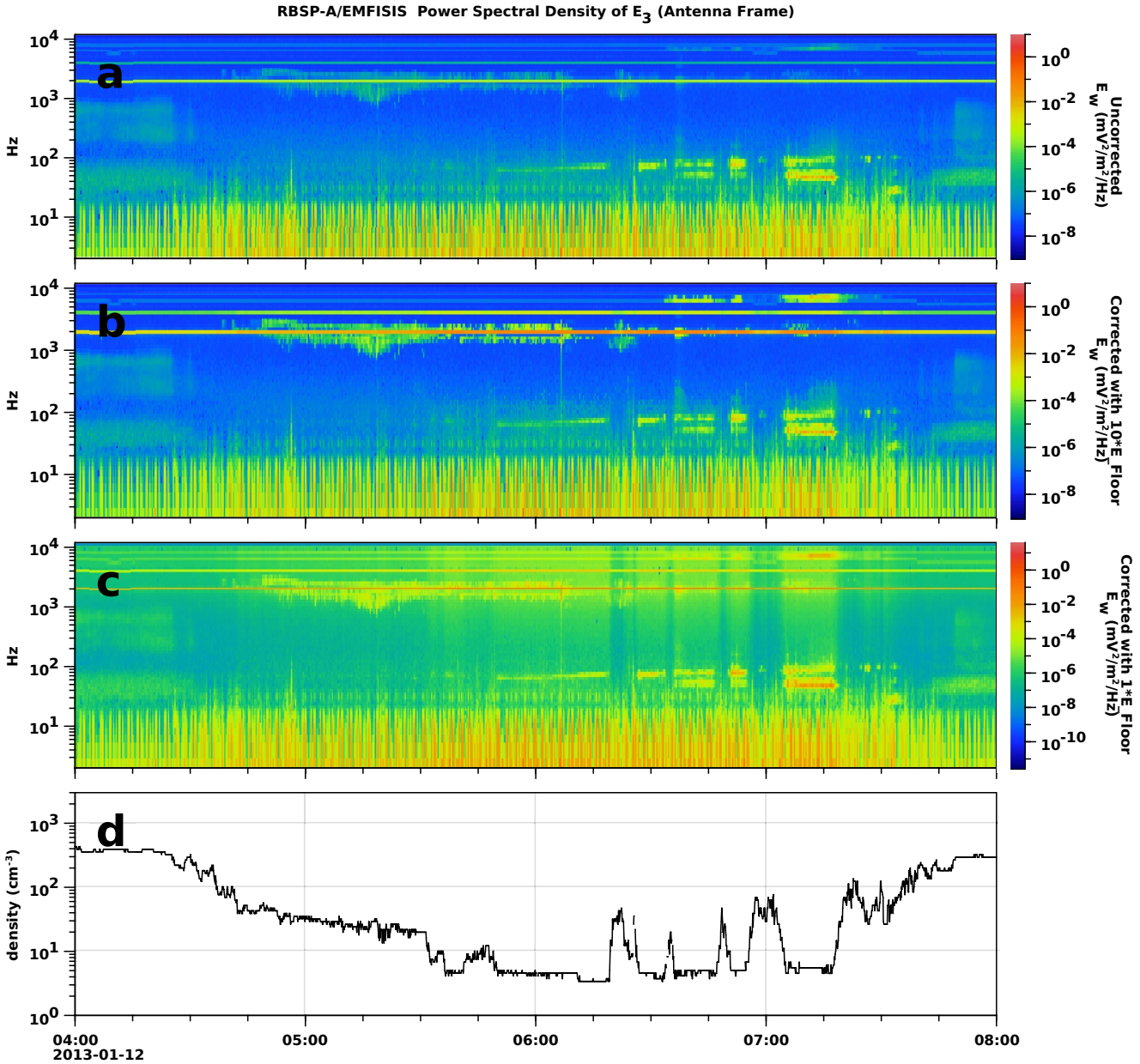

Figure 18. E_w power spectral density (PSD) for RBSP-A with (a) no sheath correction, (b) sheath correction applied where the PSD is above ten times the raw noise floor, and (c) sheath correction applied where the PSD is above the raw noise floor. (d) Plasma density during the interval.

on or off state, and the presence of this attenuation can affect the noise floor. For the majority of the mission, and almost exclusively after the first 2–3 months, this attenuator is switched on for both spacecraft. The above calculation of the noise floor therefore uses only data from that state. The same process cannot be used to find the distinct noise floors for the attenuator-off states however, as there are insufficient intervals of very quiet data available.

Instead, the noise floor for the attenuator-off states are obtained by scaling the attenuator-on noise floors. These scaling factors are obtained by identifying a handful of moderately quiet events where the attenuator state transitioned from off to on, or vice versa. The effects of these transitions on the noise floors are quantified at all frequencies, but only judged to be significant at frequencies above 2 kHz and below 7 Hz. The attenuator-off noise floor within these frequency ranges shifts downward by factors ranging from 2 to 50, depending on frequency and boom/sensor.

Finally, it should be acknowledged that these noise floors have been derived for the very specific purpose of determining when sheath corrections should be applied, and that floors used for more general science analysis would likely be calculated using a less subjective technique.

Appendix D: Applying Sheath Corrections to Spectral Matrices

The process of applying sheath corrections to spectral matrix data begins by obtaining a density value for the desired epoch from the upper hybrid resonance line as described in Kurth et al. (2015). Next, the sheath correction model is used to obtain correction factors at that density for the frequencies spanned by the spectral matrix data. Distinct corrections are used for the spin plane and spin axes.

Using empirically-derived, frequency-dependent noise floors for the spin axis and spin plane E booms/sensors, determine which spectral matrices contain E data that are a set threshold above the noise floor. This is done independently for each of the three E measurement directions. Matrices which do not pass this test will not have the correction applied for that direction, as doing so would in general artificially amplify signals which are mostly or entirely noise.

Next, decompose each 6x6 spectral matrix (one for each frequency at each epoch) into three individual 3 x 3 matricies that contain either purely B, purely E or E-B cross-terms.

$$M_B \equiv \begin{bmatrix} B_x B_x^* & B_x B_y^* & B_x B_z^* \\ \mathrm{conj}\left(B_x B_y^*\right) & B_y B_y^* & B_y B_z^* \\ \mathrm{conj}\left(B_x B_z^*\right) & \mathrm{conj}\left(B_y B_z^*\right) & B_z B_z^* \end{bmatrix} = \begin{bmatrix} B_x \\ B_y \\ B_z \end{bmatrix} \mathrm{conj}\begin{bmatrix} B_x & B_y & B_z \end{bmatrix} \tag{D1}$$

$$M_E \equiv \begin{bmatrix} E_x E_x^* & E_x E_y^* & E_x E_z^* \\ \mathrm{conj}\left(E_x E_y^*\right) & E_y E_y^* & E_y E_z^* \\ \mathrm{conj}\left(E_x E_z^*\right) & \mathrm{conj}\left(E_y E_z^*\right) & E_z E_z^* \end{bmatrix} = \begin{bmatrix} E_x \\ E_y \\ E_z \end{bmatrix} \mathrm{conj}\begin{bmatrix} E_x & E_y & E_z \end{bmatrix} \tag{D2}$$

$$M_{BE} \equiv \begin{bmatrix} B_x E_x^* & B_x E_y^* & B_x E_z^* \\ B_y E_x^* & B_y E_y^* & B_y E_z^* \\ B_z E_x^* & B_z E_y^* & B_z E_z^* \end{bmatrix} = \begin{bmatrix} B_x \\ B_y \\ B_z \end{bmatrix} \mathrm{conj}\begin{bmatrix} E_x & E_y & E_z \end{bmatrix}, \tag{D3}$$

where the second set of equalities shows the conceptually simple breakdown of each of these matrices as a product of a column and a row vector. This decomposition allows simple matrix operations to act on the E and B data independently, and thus allows the application of anything from simple scalar scalings to full vector transformations (such as coordinate system rotations).

If we let C_{sp} be the complex spin-plane correction for a given frequency and epoch, and C_{sa} the spin-axis correction, we can then construct a diagonal matrix

$$C \equiv \begin{bmatrix} C_{spx}^{-1} & 0 & 0 \\ 0 & C_{spy}^{-1} & 0 \\ 0 & 0 & C_{saz}^{-1} \end{bmatrix} \tag{D4}$$

where C_{spx} and C_{spy} are either equal to C_{sp} or equal to 1, depending upon whether or not (respectively) the E data for each of the spin-plane directions passes the noise floor test. Similarly, C_{saz} is either equal to C_{sa} or equal to 1. These corrections are then applied to the data via matrix multiplication,

$$M_{E\_corrected} = C\, M_E\, C^* \tag{D5}$$

$$M_{BE\_corrected} = M_{BE}\, C^* \tag{D6}$$

Finally, as needed, the decomposed 3 x 3 matrices can be reformed back into the standard spectral matrix format.

Appendix E: Determining Angle Between E and B in Frequency Domain

One useful application of the technique described in Appendix A is when calculating the angle between the E and B vectors using Faraday's law, when only spectral matrix data are available. Once the magnitude and relative phase of each component have been determined, we first arbitrarily set the reference phase, $\Phi(B_x)$ to zero, and then use Equation A3 to reconstruct the full complex coefficients for every component.

We then note that Faraday's law can be written

$$\vec{\mathbf{E}} \cdot \vec{\mathbf{B}} = 0, \tag{E1}$$

so using the standard expression for the dot product, we have

$$\angle EB = \arccos\left(\frac{\vec{\mathbf{E}} \cdot \vec{\mathbf{B}}}{\left|\vec{\mathbf{E}}\right| \left|\vec{\mathbf{B}}\right|}\right). \tag{E2}$$

When working with experimental wave data, this calculation will be done in the Fourier domain, using the complex coefficients output by an FFT. Needing to obtain real-valued quantities from these coefficients, the electric field magnitude is given by

$$\left|\vec{\mathbf{E}}\right| = 2\sqrt{E_x(\omega)E_x^*(\omega) + E_y(\omega)E_y^*(\omega) + E_z(\omega)E_z^*(\omega)} \tag{E3}$$

and similarly for $\left|\vec{\mathbf{B}}\right|$. The dot product is given by

$$\begin{aligned}\vec{\mathbf{E}} \cdot \vec{\mathbf{B}} = \; & 2\left[\Re\left(E_x(\omega)\right)\Re\left(B_x(\omega)\right) + \Im\left(E_x(\omega)\right)\Im\left(B_x(\omega)\right)\right. \\ & + \Re\left(E_y(\omega)\right)\Re\left(B_y(\omega)\right) + \Im\left(E_y(\omega)\right)\Im\left(B_y(\omega)\right) \\ & \left. + \Re\left(E_z(\omega)\right)\Re\left(B_z(\omega)\right) + \Im\left(E_z(\omega)\right)\Im\left(B_z(\omega)\right)\right].\end{aligned} \tag{E4}$$

The factors of 2 in Equations E3 and E4 arise by noting that the physical E and B fields are real quantities, which leads to a need for careful consideration of both the negative and positive frequency FFT coefficients when translating $\mathbf{E} \cdot \mathbf{B}$ from the time to the frequency domain.

Data Availability Statement

EMFISIS data may be obtained from http://emfisis.physics.uiowa.edu/data/index.

Acknowledgments
This work was partially performed under the support of JHU/APL contract no. 921647 under NASA Prime contract No. NAS5-01072. DPH and IWC acknowledge that this material is based upon work supported by the National Aeronautics and Space Administration under Grant No. 80NSSC21K0519 issued through the Heliophysics Guest Investigators - Open 2020 Program. OS and IK received funding from the European Union's Horizon 2020 research and innovation programme under grant agreement No. 870452 and acknowledge support from MSMT grant LTAUSA17070.

References

Bale, S. D., Ullrich, R., Goetz, K., Alster, N., Cecconi, B., Dekkali, M., et al. (2008). The electric antennas for the STEREO/WAVES experiment. *Space Science Reviews*, *136*, 529–547. https://doi.org/10.1007/s11214-007-9251-x

Boehm, M. H., Carlson, C. W., McFadden, J. P., Clemmons, J. H., Ergun, R. E., & Mozer, F. S. (1994). Wave rectification in plasma sheaths surrounding electric field antennas. *Journal of Geophysical Research*, *99*(A11), 21361–21374. https://doi.org/10.1029/94JA01766

Bonnell, J. W., Mozer, F. S., Delory, G. T., Hull, A. J., Ergun, R. E., Cully, C. M., et al. (2008). The electric field instrument for THEMIS. *Space Science Reviews*, *114*, 303–341. https://doi.org/10.1007/s11214-008-9469-2

Califf, S., & Cully, C. M. (2016). Empirical estimates and theoretical predictions of the shorting factor for the THEMIS double-probe electric field instrument. *Journal of Geophysical Research: Space Physics*, *121*, 6223–6233. https://doi.org/10.1002/2016JA022589

Cattell, C., Wygant, J. R., Goetz, K., Kersten, K., Kellogg, P. J., vonRosenvinge, T., et al. (2008). Discovery of very large amplitude whistler-mode waves in Earth's radiation belts. *Geophysical Research Letters*, *35*, L01105. https://doi.org/10.1029/2007GL032009

Cully, C. M., Ergun, R. E., & Eriksson, A. I. (2007). Electrostatic structure around spacecraft in tenuous plasmas. *Journal of Geophysical Research*, *112*, A09211. https://doi.org/10.1029/2007JA012269

Ergun, R. E., Carlson, C. W., Mozer, F. S., Delory, G. T., Temerin, M., McFadden, J. P., et al. (2001). The FAST satellite field instrument. *Space Science Reviews*, *98*, 67–91. https://doi.org/10.1007/978-94-010-0332-2_3

Fahleson, U. (1967). Theory of electric field measurements conducted in the magnetosphere with electric probes. *Space Science Reviews*, *7*, 238–262. https://doi.org/10.1007/bf00215600

Gurnett, D. A. (1998). Principles of space plasma wave instrument design. In R. F. Pfaff, J. E. Borovsky, & D. T. Young (Eds.), *Measurement Techniques in Space Plasmas Fields* (pp. 121–136). AGU. https://doi.org/10.1029/gm103p0121

Gustafsson, G., Boström, R., Holback, B., Holmgren, G., Lundgren, A., Stasiewicz, K., et al. (1997). The electric field and wave experiment for the CLUSTER mission. *Space Science Reviews*, *79*, 137–156. https://doi.org/10.1007/978-94-011-5666-0_6

Hartley, D. P., Chen, Y., Kletzing, C. A., Denton, M. H., & Kurth, W. S. (2015). Applying the cold plasma dispersion relation to whistler mode chorus waves: EMFISIS wave measurements from the Van Allen Probes. *Journal of Geophysical Research: Space Physics*, *120*, 1144–1152. https://doi.org/10.1002/2014JA020808

Hartley, D. P., Kletzing, C. A., Kurth, W. S., Bounds, S. R., Averkamp, T. F., Hospodarsky, G. B., et al. (2016). Using the cold plasma dispersion relation and whistler mode waves to quantify the antenna sheath impedance of the Van Allen Probes EFW instrument. *Journal of Geophysical Research: Space Physics*, *121*, 4590–4606. https://doi.org/10.1002/2016JA022501

Hartley, D. P., Kletzing, C. A., Kurth, W. S., Hospodarsky, G. B., Bounds, S. R., Averkamp, T. F., et al. (2017). An improved sheath impedance model for the Van Allen Probes EFW instrument: Effects of the spin axis antenna. *Journal of Geophysical Research: Space Physics*, *122*, 4420–4429. https://doi.org/10.1002/2016JA023597

Hartley, D. P., Kletzing, C. A., Santolik, O., Chen, L., & Horne, R. B. (2018). Statistical properties of plasmaspheric hiss from Van Allen Probes observations. *Journal of Geophysical Research: Space Physics*, *123*, 2605–2619. https://doi.org/10.1002/2017JA024593

Harvey, P., Mozer, F. S., Pankow, D., Wygant, J., Maynard, N. C., Singer, H., et al. (1995). *The Electric Field Instrument on the Polar Satellite in the Global Geospace Mission*. Reprinted from Space Sciences Rev. https://doi.org/10.1007/bf00751342

Khotyaintsev, Y. V., Lindqvist, P.-A., Cully, C. M., Eriksson, A. I., & Andre, M. (2014). In flight calibration of double-probe electric field measurements on Cluster. *Geoscientific Instrumentation, Methods and Data Systems*, *3*(2), 143–151. https://doi.org/10.5194/gi-3-143-2014

Kletzing, C. A., Kurth, W. S., Acuna, M., MacDowall, R. J., Torbert, R. B., Averkamp, T., et al. (2013). The Electric and Magnetic Field Instrument Suite and Integrated Science (EMFISIS) on RBSP. *Space Science Reviews*. https://doi.org/10.1007/s11214-013-9993-6

Koons, H. C., McPherson, D. A., & Harbridge, W. B. (1970). Dependence of very-low-frequency electric field antenna impedance on magnetospheric plasma density. *Journal of Geophysical Research*, *75*(13), 2490–2502. https://doi.org/10.1029/JA075i013p02490

Kurth, W. S., De Pascuale, S., Faden, J. B., Kletzing, C. A., Hospodarsky, G. B., Thaller, S., & Wygant, J. R. (2015). Electron densities inferred from plasma wave spectra obtained by the Waves instrument on Van Allen Probes. *Journal of Geophysical Research: Space Physics*, *120*, 904–914. https://doi.org/10.1002/2014JA020857

Lejosne, S., & Mozer, F. S. (2019). Shorting factor in-flight calibration for the Van Allen Probes DC electric field measurements in the Earth's plasmasphere. *Earth and Space Science*, *6*, 646–654. https://doi.org/10.1029/2018EA000550

Marklund, G. (1993). Viking investigations of auroral electrodynamical processes. *Journal of Geophysical Research*, *98*, 1691–1704. https://doi.org/10.1029/92ja01518

Marklund, G., André, M., Lundin, R., & Grahn, S. (2004). The Swedish small satellite program for space plasma investigations. *Space Science Reviews*, *111*, 377–413. https://doi.org/10.1023/b:spac.0000032690.82775.d8

Mauk, B., Fox, N. J., Kanekal, S., Kessel, R., Sibeck, D., & Ukhorskiy, A. (2012). Science objectives and rationale for the Radiation Belt Storm Probes mission. In *The Van Allen Probes Mission* (pp. 3–27). Springer. https://doi.org/10.1007/978-1-4899-7433-4_2

Mozer, F., Cattell, C., Temerin, M., Torbert, R., Von Glinski, S., Woldorff, M., & Wygant, J. (1979). The dc and ac electric field, plasma density, plasma temperature, and field-aligned current experiments on the S3-3 satellite. *Journal of Geophysical Research*, *84*(A10), 5875–5884. https://doi.org/10.1029/JA084iA10p05875

Mozer, F. S. (1973). *A proposal to measure quasi-static electric fields on the ISEE-1 mother daughter satellite* (p. 454). University of California Berkeley Space Science Technical Note.

Mozer, F. S., Agapitov, O., Krasnoselskikh, V., Lejosne, S., Reeves, G. D., & Roth, I. (2014). Direct observation of radiation-belt electron acceleration from electron-volt energies to megavolts by nonlinear whistlers. *Physical Review Letters*, *113*, 5. American Physical Society. https://doi.org/10.1103/PhysRevLett.113.035001

Mozer, F. S., Berthelier, J.-J., Fahleson, U. V., & Fälthammar, C.-G. (1974). A proposal to measure the quasi-static vector electric field on the low altitude and the elliptic orbiting electrodynamics explorer satellites. In *Research Proposal to the National Aeronautics and Space Administration*. UCBSSL No. 552/75.

Pedersen, A. (1995). Solar wind and magnetosphere plasma diagnostics by spacecraft electrostatic potential measurements. *Annales Geophysicae*, *13*, 118–129. https://doi.org/10.1007/s00585-995-0118-8

Pedersen, A., Mozer, F., & Gustafsson, G. (1998). Electric field measurements in a tenuous plasma with spherical double probes. *Measurement Techniques in Space Plasmas: Fields*, Geophysical Monograph AGU. https://doi.org/10.1029/gm103p0001

Santolík, O., & Gurnett, D. A. (2002). Propagation of auroral hiss at high altitudes. *Geophysical Research Letters*, *29*(10), 119. https://doi.org/10.1029/2001GL013666

Santolík, O., Parrot, M., & Lefeuvre, F. (2003). Singular value decomposition methods for wave propagation analysis. *Radio Science*, *38*, 1010. https://doi.org/10.1029/2000RS0025231

Santolík, O., Pickett, J. S., Gurnett, D. A., Menietti, J. D., Tsurutani, B. T., & Verkhoglyadova, O. (2010). Survey of Poynting flux of whistler mode chorus in the outer zone. *Journal of Geophysical Research*, *115*, A00F13. https://doi.org/10.1029/2009JA014925

Santolík, O., Pickett, J. S., Gurnett, D. A., & Storey, L. R. O. (2002). Magnetic component of narrowband ion cyclotron waves in the auroral zone. *Journal of Geophysical Research*, *107*(A12), 1444. https://doi.org/10.1029/2001JA000146

Storey, L. R. O. (1963). The design of an electric dipole antenna for VLF reception within the ionosphere. *Technical Reports Serie*.

Wygant, J., Bonnell, J. W., Goetz, K., Ergun, R. E., Mozer, F. S., & Bale, S. D. (2013). The electric field, and waves (EFW) instruments on the radiation belt storm probes mission. *Space Science Reviews*. https://doi.org/10.1007/s1124-013-0013-7

Wygant, J. R., Harvey, P. R., Pankow, D., Mozer, F. S., Maynard, N., Singer, H., et al. (1992). The CRRES electric field experiment/Langmuir probe. *Journal of Spacecraft and Rockets*, *29*, 601–604. https://doi.org/10.2514/3.25507